Droplet aerobreakup under the shear-induced entrainment regime using a multiscale two-fluid approach

Georgia Nykteri, Manolis Gavaises

School of Mathematics, Computer Science & Engineering, Department of Mechanical Engineering & Aeronautics, City University of London, Northampton Square EC1V 0HB, United Kingdom

Abstract

A droplet exposed to a high-speed gas flow is subject to a rapid and violent fragmentation, dominated by a widespread mist of multiscale structures that introduce significant complexities in numerical studies. The present work focuses on capturing all stages of the aerodynamic breakup of a waterlike droplet imposed by three different intensity shock waves, with Mach numbers of 1.21, 1.46, and 2.64, under the shear-induced entrainment regime. The numerical investigation is conducted within a physically consistent and computationally efficient multiscale framework, using the Σ-Y two-fluid model with dynamic local topology detection. Overall, the breakup of the deforming droplet and the subsequent dispersion of the produced mist show good agreement with available experimental studies in the literature. The major features and physical mechanisms of breakup, including the incident shock wave dynamics and the vortices development, are discussed, and verified against the experiments and the theory. While the experimental visualizations inside the dense mist are restricted by the capabilities of the diagnostic methods, the multiscale two-fluid approach provides insight into the mist dynamics and the distribution of the secondary droplets under different postshock conditions.

Keywords: droplet aerobreakup, shock wave, secondary droplets, two-fluid model, multiscale model

I. INTRODUCTION

The aerodynamic breakup of a liquid droplet imposed by a passing shock wave is a fundamental problem with a wide spectrum of engineering interest, ranging from fuel injection in both internal combustion [1], [2], [3], [4] and rocket engines [5], [6] to erosion damage in supersonic flights [7], [8]. Different classifications for the droplet breakup regimes are reported in the literature and defined based on key dimensionless parameters, namely, the Weber number (We) at free-stream conditions and the Ohnesorge number (Oh) for the liquid droplet, as follows:

$$We = \frac{\rho_g u_g^2 d_0}{\sigma}, \qquad Oh = \frac{\mu_l}{\sqrt{\rho_l \sigma d_0}},$$

with d_0 the initial droplet diameter, σ the surface tension coefficient, ρ_g the postshock gas density, u_g the postshock gas velocity, ρ_l the liquid density and μ_l the liquid dynamic viscosity.

The five classic breakup modes, known as vibrational, bag, bag-and-stamen (or multimode), sheet-stripping (or sheet-thinning) and catastrophic regime, are summarized in a We-Oh regime map for low Ohnesorge numbers (Oh << 1) in the early review studies of Hinze [9], Pilch and Erdman [10], and Faeth et al. [11]. Recently, Stefanitsis et al. [12], [13], [14] provided improved breakup models for diesel droplets within the bag, bag-and-stamen, and sheet-stripping regimes and identified an additional breakup mode, termed “shuttlecock,” which is observed during the aerodynamic breakup of droplet clusters at low Mach numbers. On the other hand, Theofanous et al. [15] reclassified the classic droplet breakup modes into two principal regimes based on the governing interfacial instabilities, namely, the Rayleigh-Taylor piercing (RTP) and the shear-induced entrainment (SIE) regime, introducing a broad and unified classification for both Newtonian and non-Newtonian droplets independent of the liquid viscosity and elasticity. Specifically, the RTP regime concerns a moderate droplet fragmentation, driven by a gradual flattening of the deforming droplet and a subsequent penetration of its accelerating mass by one or more unstable Rayleigh-Taylor waves. On the contrary, the SIE regime describes a chaotic fragmentation, defined by the prompt shear stripping from the droplet equator and followed by an extended entrainment of a multiscale mist. Dominant mechanisms that induce the droplet breakup are the Kelvin-Helmholtz instabilities, the capillary forces, and the turbulent mixing, as described by Theofanous [16]. For low viscosity liquids with Ohnesorge numbers $Oh \ll 1$, the onset of the SIE regime is established for Weber numbers above 10^3, while the transition zone between the RTP and SIE regimes occurs for moderate Weber numbers in the range of 10^2–10^3.

Early experimental investigations of the SIE regime are focused on shadowgraphy experiments of water droplets, in a first attempt to depict and explain the stripping mechanism. Engel [17] examined the fragmentation of a large (2.7 mm diameter) and a small (1.4 mm diameter) water droplet imposed by three different shock waves of Mach numbers, 1.3, 1.5, and 1.7 in order to demonstrate the influence of the sizes of rain droplets on high-speed rain-erosion damage. Additionally, Nicholls and Ranger [18] considered incident shock waves with Mach numbers up to 3.5 and investigated the role of various parameters in the droplet aerobreakup evolution, such as the droplet diameter, the breakup time, the relative velocity between the droplet and the gas stream, and the liquid-to-gas density ratio. Even though the macroscopic features of aerobreakup are revealed in both experimental studies [17], [18], namely, the liquid stripping from the droplet surface and the production of an extended mist, the shadowgraphy method imposes limitations in displaying details of the internal structure of the dense water cloud. Alternatively, pulsed laser holographic interferometry is proposed in the experiments of Wierzba and Takayama [19] and Yoshida and Takayama [20] and provides more clear and measurable visualizations of the shock-droplet interaction, the structure of the disintegrating droplet, and the formation of a wake region behind the droplet under moderate Weber numbers around 10^3 and Mach numbers between 1.3 and 1.56.

In current research, great emphasis is put on understanding the breakup mechanisms of liquid droplets, other than water droplets, of both Newtonian and non-Newtonian nature, as shown in the works of Theofanous and Li [21], Theofanous et al. [22], [23] and Mitkin and Theofanous [24]. Using laser-induced florescence (LIF), significant flow features are elucidated within a vast range of Weber and Ohnesorge numbers, including the initial Kelvin-Helmholtz waves on the coherent droplet surface and the development of different scales inside the dense mist at later stages of aerobreakup. In the case of elastic liquids, it is observed that the SIE regime is not subject to capillary forces; instead, the breakup initiates with the ruptures of extending liquid films and filaments at significantly higher Weber numbers, referred to as shear-induced entrainment with ruptures (SIER). Furthermore, recent studies in the literature investigate the effect of the postshock flow on the initiation and evolution of the aerobreakup. Wang et al. [25] examined the effect of the gas stream conditions on the macroscopic breakup pattern and the final dispersion of the produced secondary structures for a constant Weber number at 1100 and varied postshock flow Mach numbers in the range of 0.3–1.19. Specifically, the mist penetration and the fragment sizes show a dependency on the gas stream conditions and, thus, a narrower mist of less uniform fragments is observed at the advanced stages of aerobreakup under supersonic postshock conditions. Finally, Hébert et al. [26] presented experiments for significantly high Mach numbers between 4.2 and 4.6 and Weber numbers above 10^5 and defined the three stages and characteristic times of the breakup mechanism in supersonic postshock flow, namely, the droplet deformation, the extended fragmentation, and the formation of a filament from the remaining liquid mass.

An important but still little-investigated feature of the shear-induced breakup mechanism concerns the dynamics of the dense and polydisperse mist, which is forming and disintegrating as a result of the droplet fragmentation. Even with state-of-the-art laboratory apparatus available, the access to information about the dimensions of the produced structures within the mist remains challenging. The attempts to obtain droplet size distributions from high-quality experimental data visualizations in the up-to-date literature, employed by Hsiang and Faeth [27], [28], [29], Villermaux [30], and Xu et al. [31], are restricted to cases with moderate breakup, falling in the transition zone between the RTP and SIE regimes. Recent experimental studies of the SIE regime, such as the works of Theofanous [16], Theofanous et al. [22], and Wang et al. [25], provide a thorough investigation of the dominant physical mechanisms that influence the development of the dispersed mist. However, a quantification of the obtained fragment sizes inside the mist is not available.

A key characteristic of the droplet aerobreakup under the SIE regime is the broad range of spatial and temporal scales involved, which introduces additional difficulties in the accurate capturing of the overall droplet deformation and fragmentation with the available numerical methods. Two-dimensional simulations are suggested in the literature as a good compromise between the assumption of a fully symmetric droplet fragmentation and the prohibitive computational cost of a full-scale analysis. Specifically, the planar breakup of a cylindrical water column is a commonly adopted simplified problem to study the shock-imposed breakup and the shear-stripping mechanism. In the first numerical study of the entire shear-induced breakup process, Chen [32] simulated the aerobreakup of a water column after the impact with two different shock waves with Mach numbers 1.3 and 1.47, using the five-equation model of Saurel and Abgrall [33]. The simulations capture the macroscale phenomena of the droplet deformation and displacement and show good agreement with the experimental observations of Igra and Takayama [34]; however, the utilized diffuse interface approach imposes limitations regarding the sharpness of the coherent droplet interface. Similarly, with the use of the diffuse five-equation model of Allaire et al. [35], Meng and Colonius [36] provided simulations for the water column aerobreakup within a broader range of conditions with shock wave Mach numbers between 1.18 and 2.5; for the first time, the development of a recirculation region behind the deforming droplet was investigated. Sembian et al. [37] conducted new experiments and simulations with the volume of fluid (VOF) method for the early stages of the shock-water column interaction for shock wave Mach numbers 1.75 and 2.4; details of the shock wave motion are captured by the VOF method and a resolution of 440 cells per diameter. Yang and Peng [38] examined the effect of viscosity on the deformation of the liquid column, using an adaptive mesh refinement (AMR) method for higher spatial resolution. More recently, Kaiser et al. [39] performed high-resolution simulations with adaptive mesh refinement for the benchmark case of Mach number 1.47, previously simulated by Chen [32], Meng and Colonius [36], and Yang and Peng [38], with an emphasis put on the more accurate prediction of the shock wave dynamics, observed in the experiments of Igra and Takayama [40], [41]. Overall, the two-dimensional simulations of the shear-induced droplet breakup in the literature focus on the capturing of the early stages of breakup and the shock wave dynamics, without investigating the later stages of fragmentation and mist development.

Considering the high computational cost of a full-scale analysis, the limitation of the ordinary numerical methods to accurately model all different-scaled structures remains the main source of deviation between the simulation results and the experimental observations. Among the reported three-dimensional simulations in the literature to date, Meng and Colonius [42] utilized an interface capturing method and a moderate mesh resolution of 100 cells per original droplet diameter to capture the macroscopic droplet deformation and achieved good agreement with the experimental results of Theofanous et al. [22] for a shock wave Mach number 1.47 and postshock flow Weber number 780. Additionally, a Fourier analysis was performed to interpret the mechanisms of the observed surface instabilities and the subsequent ligament breakup. Liu et al. [43] conducted both axisymmetric and three-dimensional simulations to examine the aerobreakup mechanism under supersonic conditions and identified significant details of the liquid stripping and the vortices development at the early stages of aerobreakup. In an attempt to investigate water dispersion, Stefanitsis et al. [44] proposed a coupled VOF/Lagrangian approach to simulate the coherent droplet and the produced droplets cloud, respectively. The obtained results predict the detachment of microscale droplets from the coherent droplet periphery, as depicted in the experimental visualizations of Theofanous et al. [22] with, however, a lack of physical input for the sizes of the produced Lagrangian particles. Recently, an improved Eulerian/ Lagrangian model was proposed by Kaiser et al. [45] that allows a preset number of Lagrangian particles to detach from the droplet surface and, later, evolve in size, following the gas stream flow.

More sophisticated studies in the literature, including the direct numerical simulations (DNS) performed by Chang et al. [46], demonstrate the developed Kelvin-Helmholtz instabilities on the coherent droplet surface for a glycerol droplet impacted by a shock wave of Mach numbers 1.2 and 2.67. Additionally, the DNS study of Hébert et al. [26] reveals the characteristic stages and breakup times of the aerobreakup process for a water droplet under supersonic conditions with a shock wave Mach number equal to 4.24. The obtained results accurately capture the incident shock wave propagation and the subsequent bow shock formation, as observed in the experiments conducted by the same authors. However, despite the efficiency in computational resources, both DNS studies mainly focus on the early-stage dynamics and avoid investigating the dimensions of the secondary structures inside the dense water mist, which is captured as a detached but continuous filament in the simulations by Hébert et al. [26] without any internal structures .

At the same time, thorough interpretations of all the stages of aerobreakup in the current literature concern only studies with moderate Weber numbers in the transition zone between the RTP and SIE regimes, namely, with Weber numbers in the range of 10^2–10^3. Specifically, Dorschner et al. [47] presented a comprehensive analysis of the ligament formation and disintegration for the case of a water droplet exposed to a shock wave of Mach number 1.3 and a subsequent postshock flow with Weber number 470. The conducted simulations, using a multicomponent model with interface capturing and a moderate spatial resolution of 140 cells per diameter, accurately predict the recurrent breakup mechanism of the produced ligaments in consistence with the experimental observations. Additionally, in the studies of Jalaal and Mehravaran [48] and Jain et al. [49] a thorough quantitative analysis of the fragments development is demonstrated, along with information for the number of the fragments produced and secondary droplet size distributions. However, both numerical studies investigate flows with Weber numbers below 10^3 and, thus, concern the development of a relatively light mist of distinguishable larger-scaled fragments. A summary of the key numerical studies of droplet aerobreakup in the literature to date, the utilized numerical methods, the examined conditions, and the experimental works used for validation is presented in Table I. Overall, additional quantitative research is required to reveal all macroscopic and microscopic mechanisms at the later stages of breakup and provide insight into the dense mist development under the SIE regime.

Following the limitations and challenges of the commonly adopted numerical methodologies for the simulation of droplet aerobreakup, there is a gap in the literature to date concerning a detailed analysis of the dispersed mist development under the SIE regime, due to the dominance of multiscale structures and the significant computational cost of a full-scale analysis. The present study proposes the multiscale two-fluid approach, as previously developed by Nykteri et al. [50] and outlined in Section II.A., in order to investigate the multiscale features of droplet aerobreakup with a viable computational cost. The multiscale two-fluid approach employs a sharp interface method for the deforming droplet interface and a physically consistent subgrid scale modeling for the produced mist, using numerical models for the dominant subgrid scale mechanisms previously validated and utilized in the literature for similar multiscale flows and conditions [50], [51]. The proposed multiscale two-fluid approach is now utilized in the droplet aerobreakup problem and is found to predict accurately both the early-stage breakup mechanisms and the later-stage dispersion of the produced fragments imposed by three different shock waves with Mach numbers 1.21, 1.46, and 2.64, as presented in Section III and compared with the experimental observations of Theofanous [16] and Theofanous et al. [22]. The interesting aspect of the present simulations is the thorough quantitative analysis of the droplet fragmentation and the produced mist dynamics. Specifically, during the early mist development, two stripping mechanisms are identified and investigated in consistence with the experimental visualizations. Additionally, the differences in the early and later mist development under subsonic and supersonic postshock conditions are demonstrated and a physical interpretation is provided with respect to the evolution of the gas stream flow. Finally, a characterization of the droplets' population inside the dense mist is obtained and analyzed based on the modeled subgrid scale phenomena that govern the mist dynamics within the SIE regime.

Table I Summary of the key numerical studies of droplet aerobreakup in the up-to-date literature.

Year	Authors	Numerical Model	Simulation	M_s	We	Experiments
2008	Chen [32]	Five-equation model [33] (diffuse interface method)	2D planar	1.3 1.47	3.7×10^3 7.4×10^3	Igra and Takayama [34]
2012	Jalaal and Mehravaran [48]	AMR VOF method	DNS	-	38 - 400	Bremond and Villermaux [52] Cao et al. [53]
2013	Chang et al. [46]	MuSiC$^+$ solver (high-order/AMR method)	DNS	1.2 2.67	5.2×10^2 5.4×10^4	Theofanous [16]
2015	Jain et al. [49]	AMR VOF method	3D	-	20 - 120	Own
2015	Meng and Colonius [36]	five-equation model [35] (diffuse interface method)	2D planar	1.18 - 2.50	940 - 1.9×10^4	Igra and Takayama [40], [34]
2016	Sembian et al. [37]	VOF method	2D planar	1.75 2.4	9.5×10^4 3.8×10^5	Own
2018	Liu et al. [43]	Five-equation model [35] (antidiffusion method)	2D planar/3D	1.2 – 1.8 (postshock M)	$10^3 < We < 10^5$	Sembian et al. [37]
2018	Meng and Colonius [42]	Five-equation model [35] (interface capturing method)	3D	1.47	780	Theofanous et al. [22]
2019	Yang and Peng [38]	AMR sharp-interface method	2D planar	1.47	7.4×10^3	Igra and Takayama [41]
2020	Dorschner et al. [47]	Multicomponent model with interface capturing	3D	1.3	470	Own
2020	Hébert et al. [26]	Eulerian solver	2D axisymmetric/ DNS	4.24	1.2×10^5	Own
2020	Kaiser et al. [39]	AMR level-set method	2D planar	1.47	7.4×10^3	Igra and Takayama [40], [41]
2021	Kaiser et al. [45]	Eulerian/Lagrangian method	2D planar	1.47	7.4×10^3	Igra and Takayama [41]
2021	Stefanitsis et al. [44]	VOF/Lagrangian method	2D planar 3D	1.47 1.24	7.4×10^3 780	Igra and Takayama [40] Theofanous et al. [22]

II. NUMERICAL MODELING

A. Numerical method and governing equations

The Σ-Y two-fluid model with dynamic local topology detection, reported by the present authors [50], is utilized for the droplet aerobreakup simulations. The previously developed multiscale two-fluid approach consists of a broad and numerically stable case-independent multiscale framework and, thus, no modifications were required for the present simulations. Therefore, the individual features of the proposed method allow for a physically consistent and numerically stable investigation of the multiscale aspects of droplet aerobreakup within the multiscale framework. Specifically, the implemented compressible two-fluid approach, introduced by Ishii and Mishima [54], provides remarkable advantages, due to the consideration of compressibility and slip velocity effects; both flow phenomena are responsible for inducing the droplet breakup mechanism under the SIE regime. Additionally, the incorporation of the Σ-Y model, which was initially proposed by Vallet and Borghi [55], contributes to a computationally efficient full-scale analysis, since it provides modeling solutions for the microscale droplets and the underlying subgrid scale phenomena inside the widespread mist.

A fundamental feature of the multiscale framework is the topological detection of different flow regimes based on advanced on-the-fly criteria. As a result, the most appropriate modeling formulations are applied in each flow region, remaining in coherence with the local mesh resolution. Particularly in segregated flow regions, which are present on the interface of the deforming but still coherent droplet, the interface is fully resolved using the VOF sharp interface method [56], [57]. On the contrary, inside the dispersed water mist with structures smaller than the local grid size, the methodology applies a diffuse interface approach and incorporates an additional transport equation for the interface surface area density Σ [58] in order to model the unresolved subgrid scale phenomena.

The multiscale two-fluid approach has been implemented in OpenFOAM® with further developments on the twoPhaseEulerFoam solver, an available compressible, fully Eulerian implicit pressure-based solver, in order to incorporate all the additional features of the multiscale framework, namely, the interface sharpening method, the transport equation for the interface surface area density Σ, the subgrid scale models, and the switching mechanisms between the two formulations of the numerical model. In principle, the multiscale two-fluid approach consists of the same set of governing equations under both formulations, namely, the sharp and the diffuse interface approach, with specific source terms to be activated and deactivated depending on the currently operating formulation of the solver, as it is described below.

1. Two-Fluid model governing equations

The volume averaged conservation equations governing the balance of mass, momentum and energy for each phase k are

$$\frac{\partial}{\partial t}(a_k \rho_k) + \nabla \cdot (a_k \rho_k u_k) = 0\,, \tag{1}$$

$$\frac{\partial}{\partial t}(a_k \rho_k u_k) + \nabla \cdot (a_k \rho_k u_k u_k) = -a_k \nabla p + \nabla \cdot \left(a_k \boldsymbol{\tau}_k^{eff}\right) + a_k \rho_k g + \sum_{\substack{n=1 \\ n\neq k}}^{2} M_{kn}\,, \tag{2}$$

$$\frac{\partial}{\partial t}[a_k \rho_k (e_k + k_k)] + \nabla \cdot [a_k \rho_k (e_k + k_k) u_k] = -\nabla \cdot \left(a_k \boldsymbol{q}_k^{eff}\right) - \left[\frac{\partial a_k}{\partial t} p + \nabla \cdot (a_k u_k p)\right] + a_k \rho_k g \cdot u_k + \sum_{\substack{n=1 \\ n\neq k}}^{2} E_{kn}\,, \tag{3}$$

where M_{kn} represents the forces acting on the dispersed phase and depends on local topology; the surface tension force [59] is implemented under the sharp interface regime, while the aerodynamic drag force [60] is implemented under the diffuse interface regime. E_{kn} demonstrates the heat transfer between the liquid and gaseous phases, irrespectively of the flow region. More details regarding the closure of the interfacial interaction source terms are presented in the Appendix.

2. Σ-Y Model transport equations

The transport equation for the liquid volume fraction in a compressible two-phase flow is

$$\frac{\partial a_l}{\partial t} + \nabla \cdot (a_l u_m) + v_{topo}[\nabla \cdot (a_l(1-a_l)u_c)] = a_l a_g \left(\frac{\psi_g}{\rho_g} - \frac{\psi_l}{\rho_l}\right)\frac{Dp}{Dt} + a_l \nabla \cdot u_m - (1 - v_{topo})R_{a_l}\,, \tag{4}$$

where v_{topo} distinguishes between the two different interface approaches by taking either the 0 or 1 value under a diffuse or sharp interface formulation, respectively. Interface sharpness is imposed with the MULES [61] algorithm in OpenFOAM®, which introduces an artificial compression term in equation (4). Additional modifications in the governing equations for coupling the VOF method with the two-fluid framework are presented in detail in the previous work of the authors [50]. Finally, as discussed in the works of Vallet et al. [62] and Andreini et al. [51], the term R_{a_l} accounts for the liquid dispersion induced by turbulent velocity fluctuations, which are important in dispersed flows and smaller scales.

The transport equation for the liquid gas interface surface area density Σ [58] is described as

$$\frac{\partial \Sigma'}{\partial t} + \nabla(\Sigma' u_m) = (1 - v_{topo})\left[-R_\Sigma + C_{SGS}\frac{\Sigma}{\tau_{SGS}}\left(1 - \frac{\Sigma}{\Sigma^*_{SGS}}\right)\right], \tag{5}$$

where the simultaneous existence of liquid and gas on the interface implies the presence of a minimum interface surface area density, such as $\Sigma = \Sigma' + \Sigma_{min}$, as shown by Chesnel et al. [63]. The term R_Σ represents the interface surface area diffusion due to turbulent velocity fluctuations, as derived by Andreini et al. [51]. The subgrid scale (SGS) source term, namely, the term $S_{SGS} = C_{SGS}\frac{\Sigma}{\tau_{SGS}}\left(1 - \frac{\Sigma}{\Sigma^*_{SGS}}\right)$, accounts for all physical mechanisms which are responsible for local interface formation and fall below the computational mesh resolution. Details regarding the closure of the SGS source term are presented in the Appendix.

Knowing the interface surface area density, the diameter of a droplet inside the dispersed mist d_Σ is calculated as the equivalent diameter of a spherical particle which has the same volume to surface area ratio as the examined computational cell, proposed by Chesnel et al. [63]:

$$d_\Sigma = \frac{6a_l(1-a_l)}{\Sigma}, \tag{6}$$

where α_l represents the liquid volume fraction and Σ the total liquid gas interface surface area density, calculated in equation (5).

3. Flow topology detection algorithm

The implemented flow topology detection algorithm identifies instantaneous topological changes in flow regimes, evaluates the most appropriate numerical treatment for local interfaces, and allows for a flexible and stable two-way switching between the sharp and diffuse interface approaches. The topological switching criteria are described in detail in the previous work of the authors [50].

B. Problem definition and simulation setup

The droplet aerobreakup is examined for a waterlike droplet with an initial diameter of 1.9 mm, namely, a tributyl phosphate (TBP) droplet with density ρ=978 kg/m³ and dynamic viscosity $\mu=4\times10^{-3}$ Pa·s, similar to water properties, but a very low surface tension of σ=0.027 N/m. The numerical simulations are conducted for three different shock waves that impact the droplet and correspond to a subsonic, transonic, and supersonic postshock gas stream. The simulation results are compared with the experimental observations of Theofanous [16] and Theofanous et al. [22] for the same aerobreakup cases. The three examined cases comprehensively cover the range of the available experimental conditions for low viscosity liquids within the SIE regime in the literature, as depicted in the regimes map in [22]; the onset of the SIE regime is defined for Weber numbers greater than 10^3 and demonstrates a moderate shear-induced aerobreakup, while the most intense and violent fragmentation is observed for significantly higher Weber numbers above 10^5 and supersonic postshock flow conditions.

Table II summarizes the Mach numbers of the propagating shock waves, the postshock flow conditions, and the Weber and Reynolds numbers calculated for the gas properties at postshock conditions. The postshock gas stream properties are also used for the nondimensionalization of the flow fields, as shown in Meng and Colonius [42], in order to obtain a direct comparison between the different cases.

Table II Shock wave and postshock conditions for the conducted droplet aerobreakup simulations.

case	$\mathbf{M_s}$	$\mathbf{p_s}$ [Pa]	$\mathbf{T_s}$ [K]	$\boldsymbol{\rho_s}$ [kg/m^3]	$\mathbf{u_s}$ [m/s]	**We**	**Re**
1	1.21	156187	340.4	1.6	110.87	1.6×10^3	1.6×10^4
2	1.46	235094	388	2.11	224.97	7×10^3	3.7×10^4
3	2.64	807006	683.9	4.11	654.9	1.23×10^5	1.6×10^5

The droplet aerobreakup simulations are performed in a two-dimensional (2D) axisymmetric geometry with one cell thickness in the azimuthal direction, using two computational meshes with a resolution of 100 and 200 cells per original droplet diameter around the area of interest. The computational domain is sufficiently large to avoid nonphysical reflections on the borders and Neumann boundary conditions are applied for all the computed flow fields. The simulations are initiated with the shock wave being one diameter away from the center of the droplet. Details of the initial configuration and the computational mesh are illustrated in Figure 1.

DNS studies in the literature [43], [46] utilized a computational mesh of more than 1000 cells per diameter to solve the viscous boundary layer and predict the Kelvin-Helmholtz instabilities. However, due to the significant computational cost, these DNS studies are restricted to the demonstration of the early-stage instabilities on the coherent droplet surface and do not examine the later-stage fragmentation and mist development, which is the main objective of the current simulations. On the contrary, the utilized spatial resolution of 100 and 200 cells per original diameter is commonly selected in the literature, for instance in the simulations of [26], [42], [44], [47], and is proven to capture accurately the macroscopic deformation of the coherent droplet surface, while the investigation of the Kelvin-Helmholtz instabilities remains out of scope in the present study.

The two characteristic scales that determine the onset of the droplet aerobreakup under the SIE regime are the characteristic viscous velocity $u_V^+ = \frac{\nu_l}{d_0} \cong 9\times10^{-6}\ m/s$ and the characteristic capillary velocity $u_C^+ = \sqrt{\frac{\sigma}{d_0\rho_l}} \cong 0.12\ m/s$, as defined by Theofanous [16]. The viscous velocity is related to the unresolved Kelvin-Helmholtz instabilities inside the viscous boundary layer, while the capillary velocity balances the stripping actions of the developed wake on the droplet surface and the surface tension force that restrains the liquid detachment. With respect to the characteristic scales of turbulence, the Kolmogorov velocity scale is around ~0.1 m/s in subsonic case 1 and it rises to ~1 m/s in supersonic case 3. At the same time, the secondary droplets produced inside the mist have diameters in the range of 0.01–19 μm, while the Kolmogorov length scale is of the order of ~0.5 μm in the three examined cases. Therefore, turbulence effects are becoming more significant under supersonic postshock conditions and are responsible for the breakup of the smallest-scaled droplets.

In the present simulations, the flow turbulence is considered using Large Eddy Simulations (LES) with the implementation of the one-equation SGS model of Lahey [64]. However, the utilized 2D axisymmetric geometry with one cell thickness in the azimuthal direction imposes limitations regarding the accurate capturing of the turbulent state, which corresponds to fully three-dimensionally (3D) developed phenomena. Specifically, the simulation is initialized without turbulence in the flow field and, thus, the instantaneous velocity field is 2D. Therefore, in the absence of developed turbulence or a developed turbulent boundary layer at the initial conditions, the LES approximation can be applied in the present geometry of one cell thickness in the azimuthal direction without significant limitations. Additionally, Stefanitsis et al. [65] depicted that the assumption of a symmetrical flow field around the deforming droplet under the influence of turbulence and vortex shedding does not affect the shape of the coherent droplet; however, it can have an influence on the trajectory and the breakup time of the fragments. Hence, the present axisymmetric geometry can adequately predict the coherent droplet deformation and fragmentation with minor limitations regarding the produced fragments' motion due to the absence of the stochastic character of a fully developed turbulent field. At the same time, key numerical studies in the literature [26], [36], [42], [43], [39] exclude the consideration of turbulence effects, without a limitation in capturing the dominant macroscopic phenomena of the aerobreakup evolution, while DNS studies [26], [46] do not report any significant difference or previously unrevealed mechanisms in the flow field due to the resolved turbulence. Consequently, despite the discussed limitations, the utilized 2D axisymmetric geometry with one cell thickness in the azimuthal direction is an acceptable compromise between an adequate turbulence model and a viable computational cost.

Regarding the numerical simulation setup, the spatial discretization used is based on second-order accurate discretization schemes. Time stepping is performed adaptively during the simulation to respect the selected limit for the convective Courant–Friedrichs–Lewy (CFL) condition of 0.2. Finally, the thermodynamic closure of the system is achieved by implementing the stiffened gas equation of state, proposed by Ivings et al. [66], for the liquid phase and the ideal gas equation of the state for the gaseous phase, which can perform adequately even under supersonic postshock conditions, as shown in Hébert et al. [26].

III. RESULTS AND DISCUSSION

The numerical investigations of the droplet aerobreakup using the proposed multiscale two-fluid approach are presented for the three cases of Table II in Figures 2-4, respectively, and compared with the corresponding experimental observations of Theofanous [16] and Theofanous et al. [22]. Following the pass of the shock wave, the small-scale interfacial instabilities on the droplet surface and the pressure differences between the upstream and downstream side of the droplet impose a gradual deformation of the initially spherical droplet into a flattened shape. The deforming coherent droplet interface is captured using the VOF method and illustrated with red isolines in Figures 2(i), 3(i), and 4(i). As can be observed for the three simulated cases, the macroscopic deformation of the coherent droplet interface shows a good qualitative agreement with the experimental results, following satisfactorily the spanwise expansion and the flattening of the back side of the droplet.

At the same time, the large-scale droplet deformation is followed by an extended fragmentation, which initiates due to liquid stripping from the droplet surface and results in the formation of a dispersed mist of microscale structures. The produced mist is simulated within the diffuse interface formulation of the multiscale framework, while numerical models are introduced for consideration of the unresolved subgrid scale phenomena. Specifically, during the early stages of aerobreakup, liquid stripping is observed initially from the droplet equator and later from the back side of the droplet with the two streams colliding into a primary stream and forming a widespread mist, as shown in Figures 2(i), 3(i), and 4(i) and previously discussed in the study of Liu et al. [43]. The main stripping mechanism, which is responsible for the production of the primary stream, is enhanced by the growing vortices formed on the back side of the droplet; the vortices interact with the droplet surface and enhance the existing mist with additional fragments, as illustrated in Figures 2(iv), 3(iv), and 4(iv). Even though the near-stagnation region remains relatively flat, as observed in the experimental visualizations of Theofanous [16] and Theofanous et al. [22], a secondary stream of fragments is detached from the front side of the droplet. Unlike the main stripping mechanism, which is dominated by the local flow vorticity, the secondary stripping mechanism is acting on the high-pressure side of the droplet and is driven by the interfacial instabilities on the droplet surface, the strong shear, and the aerodynamic conditions around the droplet. As a result, the produced secondary stream is more pronounced with an increase of the incident shock wave Mach number, as observed in Figure 4(i), since the supersonic postshock conditions impose higher local pressure and gas stream velocities and, thus, amplify the aerodynamic forces on the front side of the droplet. Finally, the primary and secondary streams of fragments merge, following the free-stream gas flow and the aerodynamic force imposed by the upstream and downstream pressure differences, and create a dense mist layer around the deforming droplet in consistence with the experimental observations. At the late stages of fragmentation, secondary structures continue to detach from the surface of the elongated but still coherent body of the deformed droplet, while the penetration and dispersion of the produced mist dominate the breakup mechanism.

The dimensions of the produced droplets inside the dense mist are obtained in coherence with the evolution of the interface surface area, considering turbulence, droplet collision and coalescence, and secondary breakup effects within the multiscale framework. The largest secondary droplets with a maximum diameter of 19 μm are detected close to the coherent droplet and on average around the droplet equator and the droplet flattened back side, as illustrated in Figures 2(iii), 3(iii), and 4(iii). Thus, based on the liquid stripping mechanism, the largest captured secondary droplets are detached from the coherent droplet under the influence of the main stripping mechanism and are embedded in the primary stream of fragments. Additionally, in the supersonic case 3 in Figure 4(iii), significantly large droplets close to the maximum diameter are also observed on the droplet front side during the later stages of fragmentation, when the secondary stripping mechanism contribution to the overall droplet aerobreakup is remarkable. The maximum diameter is correlated with the local mesh resolution for a mesh of 100 cells per initial diameter and, thus, the size limit for structures that can be resolved with the VOF method. Details about the upper limit of the subgrid diameters with respect to the local grid resolution are presented in the Appendix. In the review study of Pilch and Erdman [10], the largest fragments detached from the droplet equation are approximately one to two orders of magnitude smaller than the original droplet, which is in agreement with the newly detached fragments captured by the multiscale two-fluid approach. At the same time, the smallest subgrid scale droplets observed downstream have diameters in the range of 0.01–0.1 μm, without the numerical model to impose a lower diameter limit. These microscale droplets are visible as a cloud but cannot be quantified in the experiment and, thus, there is no experimental input for the smallest droplet sizes. However, the significant extent of the secondary droplets' interactions inside the dense mist can justify the production of the detected smallest sizes, while the exclusion of vaporization effects from the performed simulations can be related with the possible longer-term presence of the smallest secondary droplets inside the dense mist. During the earlier stages of aerobreakup, the small-scale secondary droplets with diameters below 1 μm are mostly observed downstream at the edges of the forming mist. Later, these are trapped inside the extended mist that continuously increases in volume and recirculates behind the deforming droplet.

A driving mechanism for the aerodynamically imposed breakup and characteristic feature of the water dispersion evolution is the recirculation of the produced secondary droplets within the water mist. As depicted in Figures 2(iv), 3(iv), and 4(iv) and discussed in the simulations of Meng and Colonius [42], the interaction of two counter-rotating vortices is the key mechanism for the formation of a dominant wake recirculation region behind the deforming droplet. In the course of fragmentation, more secondary vortices with varying length scales and spatial arrangement form in the wake between the convex front side and the flattened back side of the coherent droplet and are responsible for its deforming shape. Focusing on the effect of the propagating shock wave on the dynamics of the produced water mist, an increased Mach number results in a postshock flow with an extended streamwise but relatively limited spanwise recirculation zone behind the droplet, as illustrated in Figures 2(iv), 3(iv), and 4(iv). The free-stream gas velocity shows similar behavior irrespectively of the Mach number with maximum values up to 1.5 times the initial postshock velocity, observed in the region above the droplet equator and extending downstream along the negative vorticity side of the primary wake. At the same time, the secondary droplets that are subject to a vortical flow show maximum and minimum velocity values in antidiametrical positions along the primary recirculation region independent of the underlying droplet sizes. As highlighted in Figures 2(iv), 3(iv), and 4(iv), the maximum velocity values are observed for the secondary droplets located along the upper and lower side of the primary wake, while the minimum velocity values are found above the droplet back side and downstream on the right side of the primary wake. Following the dominance of the vortical mechanism over time, the maximum velocity values among the secondary droplets gradually increase, until they reach or even slightly exceed the gas steam velocity values at the initial postshock conditions, namely, 110.87, 224.97, and 654.9 m/s, for cases 1, 2, and 3, respectively. While the minimum velocity values in the droplets' recirculation region approach zero, the newly detached fragments from the back side of the droplet do not remain stagnant. Nevertheless, they are embedded in the primary stream of fragments that is continuously enhanced and governed by the developed flow vorticity.

Focusing on the early-stage deformation in Figure 5, the droplet surface isolines, obtained from the experimental results in the work of Theofanous et al. [22], are compared against the numerical isolines for two different mesh resolutions of 100 and 200 cells per initial droplet diameter. The droplet surface deformation is adequately predicted by the conducted simulations and only minor deviations from the experimental isolines are observed on the tip of the flattened back side of the droplet, where the numerical method already detects detached fragments, as depicted in Figures 2-4. Additionally, the good agreement between the simulation results with the utilization of a coarse and a fine computational mesh demonstrates that a moderate mesh resolution of 100 cells per initial diameter is sufficient to resolve the large-scale droplet deformation. The sharpness of the numerical solution is examined in Figure 6, obtaining the droplet surface isolines from different values of the liquid volume fraction and considering more advanced droplet deformation. As illustrated in Figure 6, the coherent droplet interface remains sufficiently sharp even at the late stages of aerobreakup. Some minor differences are observed on the upper tip of the deformed droplet interface and the detached large-scale secondary droplets.

The intensity of the incident shock wave imposes the occurring postshock flow conditions and is crucial for the droplet deformation and the consequent water dispersion. In the subsonic case, shown in Figure 7(a), when the shock wave with Mach number 1.21 impacts the stagnant droplet, the local pressure increases at approximately 2 bars. At the same time, the incident shock wave continues to propagate downstream, and a reflected shock wave is established on the front side of the droplet and initiates its upstream propagation. The developed postshock flow conditions are characterized by moderate pressure difference around the droplet and maximum local Mach number values at about 0.45. The transonic case of Figure 7(b) shows similar behavior; however, the slower propagation of the reflected shock wave and the higher local Mach numbers lead to a more widespread fragmentation. On the contrary, in the supersonic case of Figure 7(c) the strong shock wave with Mach number 2.64 results in a significant increase of the local pressure at 35 bars after impact. The subsequent reflected shock wave stabilizes close to the droplet as a detached bow shock. As a result, the flow conditions around the droplet remain supersonic with maximum local Mach number values above 2 that impose a significantly faster and more violent droplet fragmentation, which appears as a very dense and extensive dispersed mist downstream, also observed in the experiments of Hébert et al. [26] for similar Weber numbers.

The widespread water dispersion in the form of a dense mist is the major fragmentation pattern under the SIE regime. An insight into the dimensions of the produced secondary droplets within the mist is presented in Figure 8, depicting the volume concentration of different droplet classes over the total volume of the dispersed region, as captured by the numerical model for the three cases in Table II. A significant advantage of the conducted numerical simulations is the consideration of every fluid structure that forms as part of the flow development without excluding small sizes, thus providing information for sizes below the 5μm/pixel resolution of the camera utilized in the reported experiments and illustrated in gray in Figure 8. The first secondary droplets produced in all three cases are small structures, with more than 60% of the diameters in the total volume being below 1 μm; these droplets are forming due to the initial liquid stripping from the droplet equator, as observed in the experiments at the very early stages of aerobreakup. Shortly after, the large-scale fragmentation is established when droplets with diameters above 5 μm are detached from the coherent droplet surface and, thus, an additional class of larger droplets, colored in gray, is included in the distributions of Figure 8 at 42, 20, and 7.1 μs for the cases 1, 2, and 3, respectively.

Considering the evolution of the population of secondary droplets over time, larger droplet sizes above 1 μm become more significant in the population with increasing Mach number, as observed in Figure 8 for cases 2 and 3. There are two crucial parameters that influence the secondary droplets' distribution–first, the sizes of the newly detached fragments from the coherent droplet surface and, second, the subgrid scale droplet interactions inside the existing dispersed mist. Specifically, an increase of the incident shock wave Mach number imposes a violent droplet fragmentation with extended liquid stripping from the droplet surface due to severe aerodynamic conditions around the droplet and the dominance of the secondary stripping mechanism. As a result, large-scale droplets continue to fragment from the coherent droplet surface and enhance the secondary droplets population even during advanced stages of the aerobreakup process, as depicted in the distributions of Figure 8(ii) and 8(iii) for the class of the largest droplets with diameters between 5 and 19μm and also illustrated in Figures 3 and 4 for the indicated time instances.

Following the production of the new fragments, the subgrid scale droplet interactions are responsible for the further evolution of the secondary droplet sizes inside the dispersed mist. The required subgrid scale modeling is performed within the multiscale framework using the transport equation for the interface surface area, equation (5); the mechanisms that determine the local interface formation, namely, turbulent mixing, droplet collision and coalescence, and secondary breakup effects, are modeled as individual source terms S_{SGS}. A positive contribution of the SGS source term corresponds to an increase of the local interface surface area and physically correlates with the evolution of the underlying subgrid scale droplets into smaller diameters, while a negative SGS source term value describes a decrease of the local interface surface area due to the creation of subgrid scale droplets with larger diameters. The secondary breakup mechanism can only result in the further breakup of the existing secondary droplets inside the mist and, thus, has only a positive contribution in the SGS source term. Details regarding the calculation of the SGS source term are presented in the Appendix.

Figure 9 represents the volume concentration of the three subgrid scale mechanisms that contribute positively to the local interface surface area production and the creation of smaller-scaled droplets, namely the flow turbulence, droplet collision, and secondary breakup effects, over the total volume of the dispersed region, as calculated in equation (5) for the three examined cases. In case 1, the subgrid scale turbulence and collision effects contribute to the production of the local interface surface area by above 90%, already at the early stages of aerobreakup, while the secondary breakup effects, governed by the relative velocity between the liquid and gaseous phases, are absent under the subsonic postshock conditions. Overall, the predominant pattern is the further decrease of the secondary droplets' sizes inside the dispersed mist, which is also reflected in the droplet population in Figure 8(i), highlighting an increase and dominance of the smallest scales over time. A distribution of uniformly small-scaled fragments is also demonstrated in the experiments of Wang et al. [25] at subsonic postshock flows. In case 2, shown in Figure 9(ii), the creation of smaller-scaled droplets, driven by the local turbulence and collision, remains dominant for the mist evolution with a minor decrease compared to case 1. Additionally, the secondary breakup mechanism is not completely absent and has a small contribution in the mist dynamics. Therefore, the slightly reduced concentration of the class of droplets with the smallest diameters below 1 μm, as depicted in the distribution in Figure 8(ii), is a combination of the enhancement of the larger-scaled new fragments under the transonic postshock conditions and the small decrease of the subgrid scale interface surface area production.

Finally, case 3, presented in Figure 9(iii), demonstrates the significant influence of the supersonic postshock conditions on the subgrid scale mechanisms. Specifically, even though the flow turbulence maintains a major positive contribution to the production of smaller-scaled droplets, the collision effects are remarkably reduced by coalescence that becomes significant after the early stages of aerobreakup, even before the width of the deforming droplet is decreased by 10%. The coalescence of the secondary droplets enhances the droplet population with larger-scaled droplets and explains the decreased concentration of the droplet class with the smallest diameters, observed approximately after 10 μs in Figure 8(iii). As illustrated in Figure 10, coalescence effects are present in the region of the main stripping mechanism, namely, close to the droplet equator and the back side of the deforming droplet. During the evolution of aerobreakup, the coalescence region expands, driven by the increasing local flow vorticity. Similarly, in the study of Wang et al. [25], the presence of larger fragments among the dominant microdroplets is observed at the advanced stages of aerobreakup under supersonic postshock conditions. As discussed in [25] and in agreement with the present subgrid scale analysis, these nonuniform fragments coalesce into larger secondary droplets, as imposed by the local flow conditions and the limited spanwise spread on the produced dense mist. At the same time, the secondary breakup shows a considerable and gradually increasing contribution to the mist evolution over time, as depicted in Figure 9(iii). The secondary breakup mechanism is mainly established on the droplet front side, shown in Figure 10, where the secondary stripping mechanism dominates and the relative velocity between the newly detached droplets and the supersonic gas flow locally exceeds the value of 200 m/s. However, the secondary breakup of subgrid scale droplets is not contributing significantly to the increase of the population of the smallest droplets, since it involves, on average, the breakup of large-scaled droplets with diameters above 2 μm, as demonstrated in Figure 10 for the time instances that correspond to a decrease for the width of the deforming droplet by 10%, 25%, and 50%.

Lastly, the volume concentration of the water mist over the total volume of the water phase is reduced by approximately 10% in case 3 compared to the lower Mach number cases 1 and 2 for the same width deformation, as shown in Figure 8(iii). At the early stages of aerobreakup, the limited mist concentration is related with the postponed breakup initiation, also observed in the experiments of Wang et al. [25] at supersonic postshock conditions. However, at the later stages of aerobreakup, the stripping mechanism becomes more significant under the influence of both the main and the secondary stripping mechanisms, depicted in Figure 6 in comparison with cases 1 and 2, leading to an extended and violent stripping from the coherent droplet surface. On the contrary, during the later stages of the aerobreakup process, the mist dynamics, governed by the modeled subgrid scale mechanisms, play a major role in the evolution of the dispersed mist. In particular, as highlighted in Figure 9(iii) and discussed previously, the remarkable coalescence effects result in the destruction of the local interface surface area and, thus, act against the further expansion of the existing mist. At the same time, the violent fragmentation under the supersonic postshock conditions along with the increasing flow vorticity behind the deforming droplet impose the mist into a rapid downstream penetration. Therefore, the expansion of the dispersed mist in the spanwise direction is restricted compared to the cases with lower Mach numbers due to the severe gas stream conditions. Likewise, in the experiments of Wang et al. [25] a significantly narrower mist expansion is observed at supersonic conditions. In conclusion, the supersonic postshock conditions impose the development of a relatively reduced mist with the significant presence of larger-scaled droplets until the advanced stages of aerobreakup.

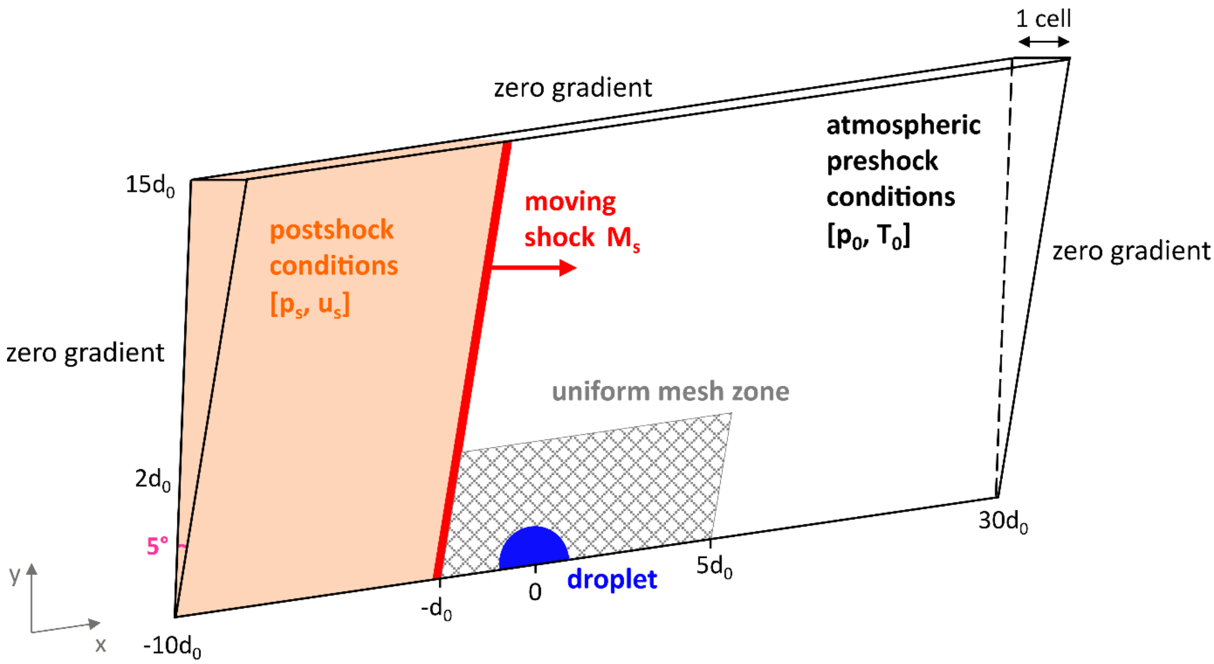

Figure 1 Initial configuration and information regarding the computational mesh for the simulation of droplet aerobreakup.

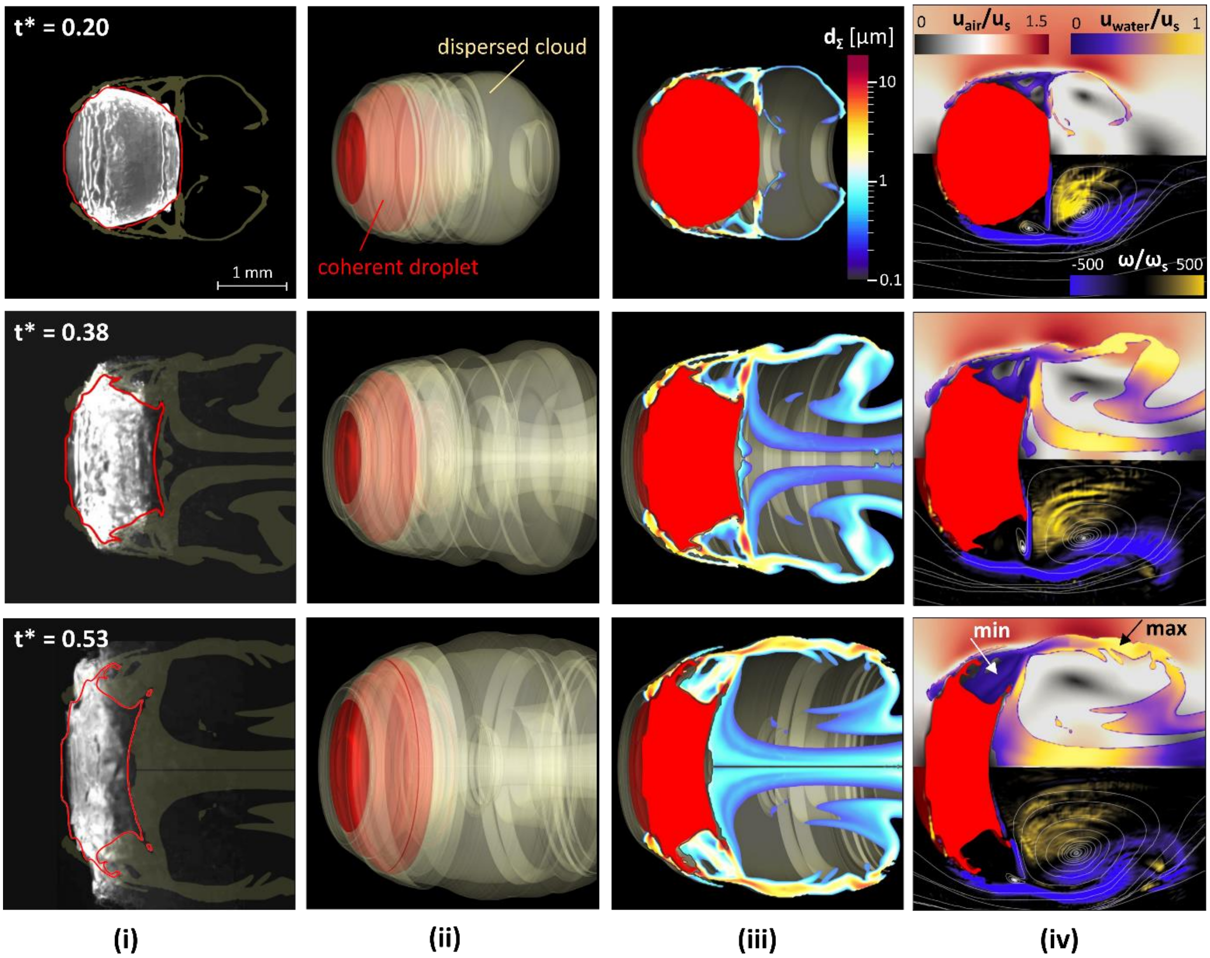

Figure 2 Droplet aerobreakup in case 1. (i) Comparison between the experimental visualizations of Theofanous et al. [22] (t*=0.20, 0.38) and Theofanous [16] (t*=0.53), the simulation results of the deforming coherent droplet (red isoline for water volume fraction value 0.5), and the produced water mist (yellow isosurface for water volume fraction values higher than 10^{-5}). (ii) 3D reconstructed results. (iii) Dimensions of the secondary droplets inside the mist. (iv) Air and water velocity magnitudes (top) and vorticity streams (bottom).

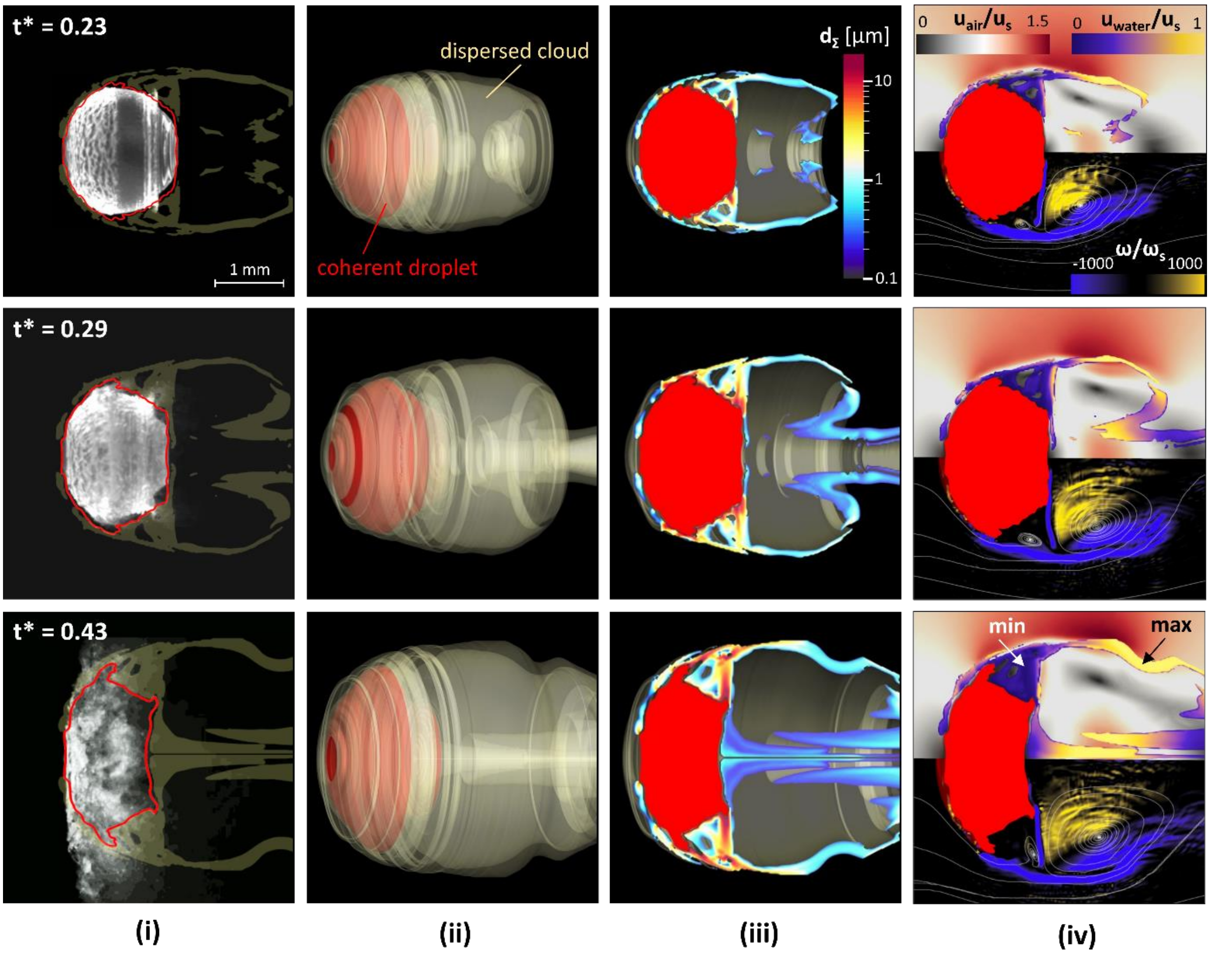

Figure 3 Droplet aerobreakup in case 2. (i) Comparison between the experimental visualizations of Theofanous et al. [22] (t^*=0.23) and Theofanous [16] (t^*=0.29, 0.43), the simulation results of the deforming coherent droplet (red isoline for water volume fraction value 0.5), and the produced water mist (yellow isosurface for water volume fraction values higher than 10^{-5}). (ii) 3D reconstructed results. (iii) Dimensions of the secondary droplets inside the mist. (iv) Air and water velocity magnitudes (top) and vorticity streams (bottom).

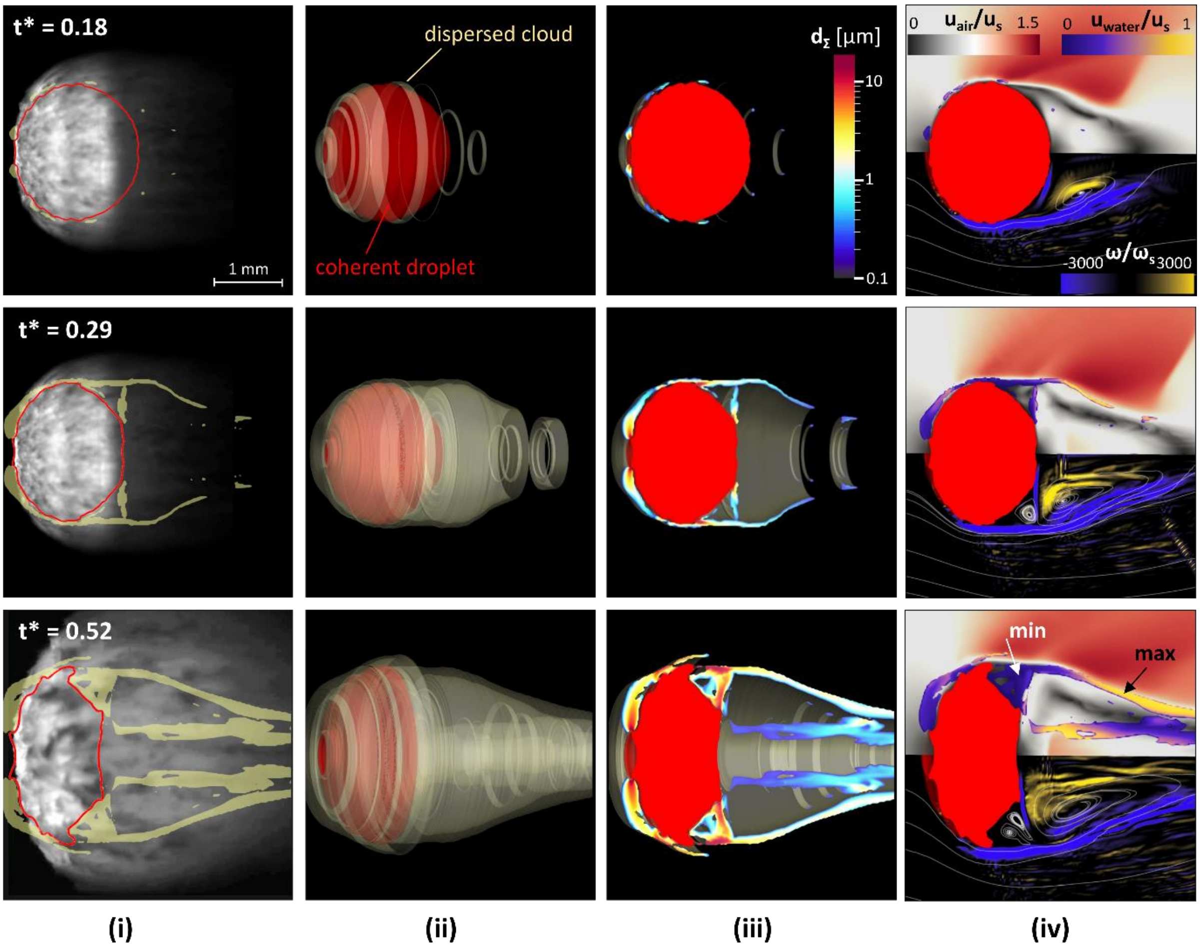

Figure 4 Droplet aerobreakup in case 3. (i) Comparison between the experimental visualizations of Theofanous et al. [22] (t^*=0.18, 0.29) and Theofanous [16] (t^*=0.52), the simulation results of the deforming coherent droplet (red isoline for water volume fraction value 0.5), and the produced water mist (yellow isosurface for water volume fraction values higher than 10^{-5}). (ii) 3D reconstructed results. (iii) Dimensions of the secondary droplets inside the mist. (iv) Air and water velocity magnitudes (top) and vorticity streams (bottom).

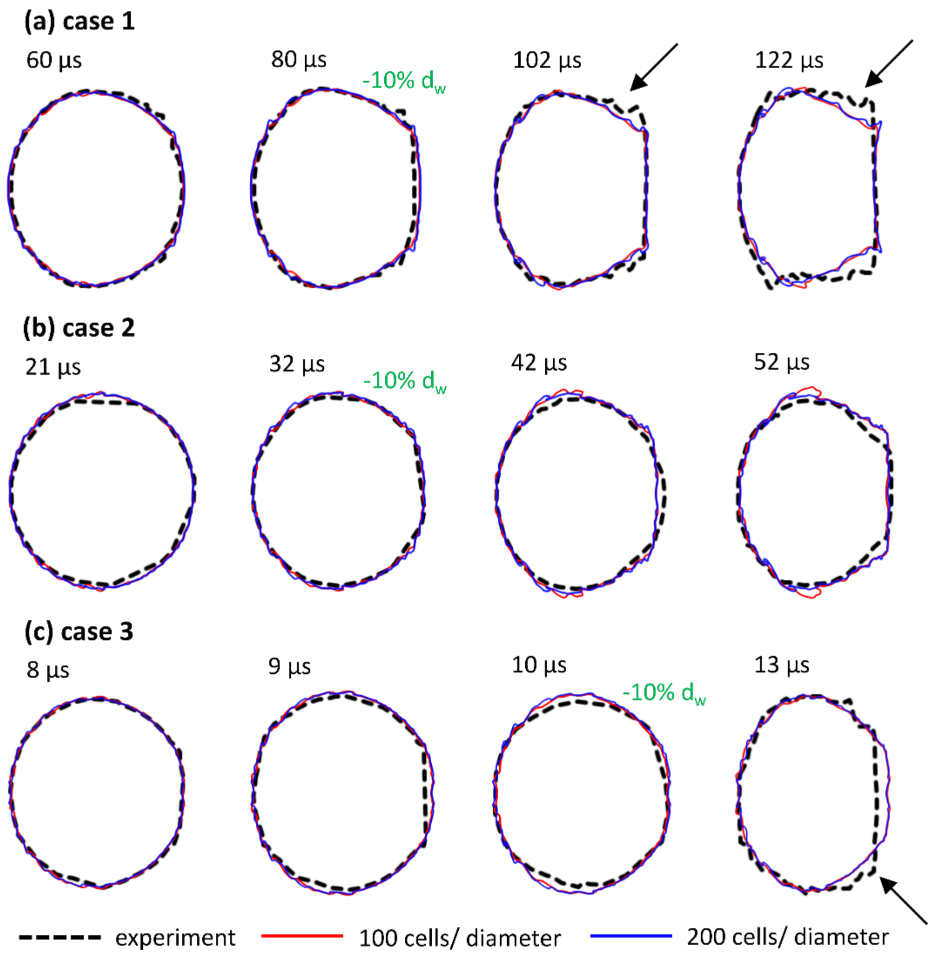

Figure 5 Coherent droplet isolines. Comparison between the experimental isolines of Theofanous et al. [22] (black dashed line) and the simulation isolines for volume fraction value 0.5 using a computational mesh with 100 (red solid line) and 200 (blue solid line) cells per initial droplet diameter. The arrows point to the small deviations between the experimental and simulation isolines.

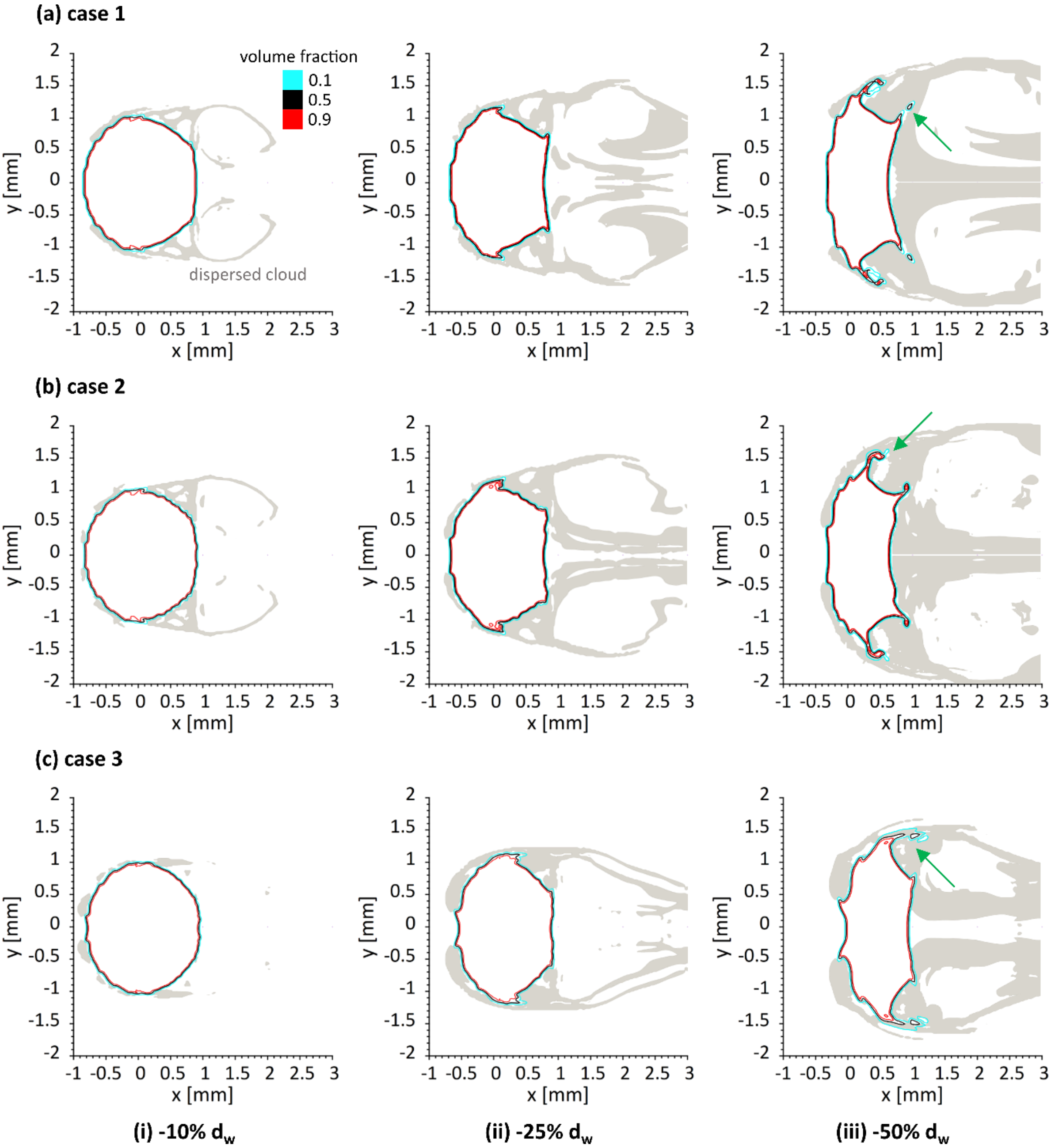

Figure 6 Coherent droplet isolines for different water volume fraction values, using a computational mesh with 100 cells per initial droplet diameter. Produced water mist isosurface for water volume fraction values higher than 10^{-5} (gray). Comparison between cases 1, 2, and 3 at time instances that correspond to a decrease for the width of the deforming droplet by 10%, 25%, and 50%. The arrows point to the small deviations in interface sharpness with different volume fraction values.

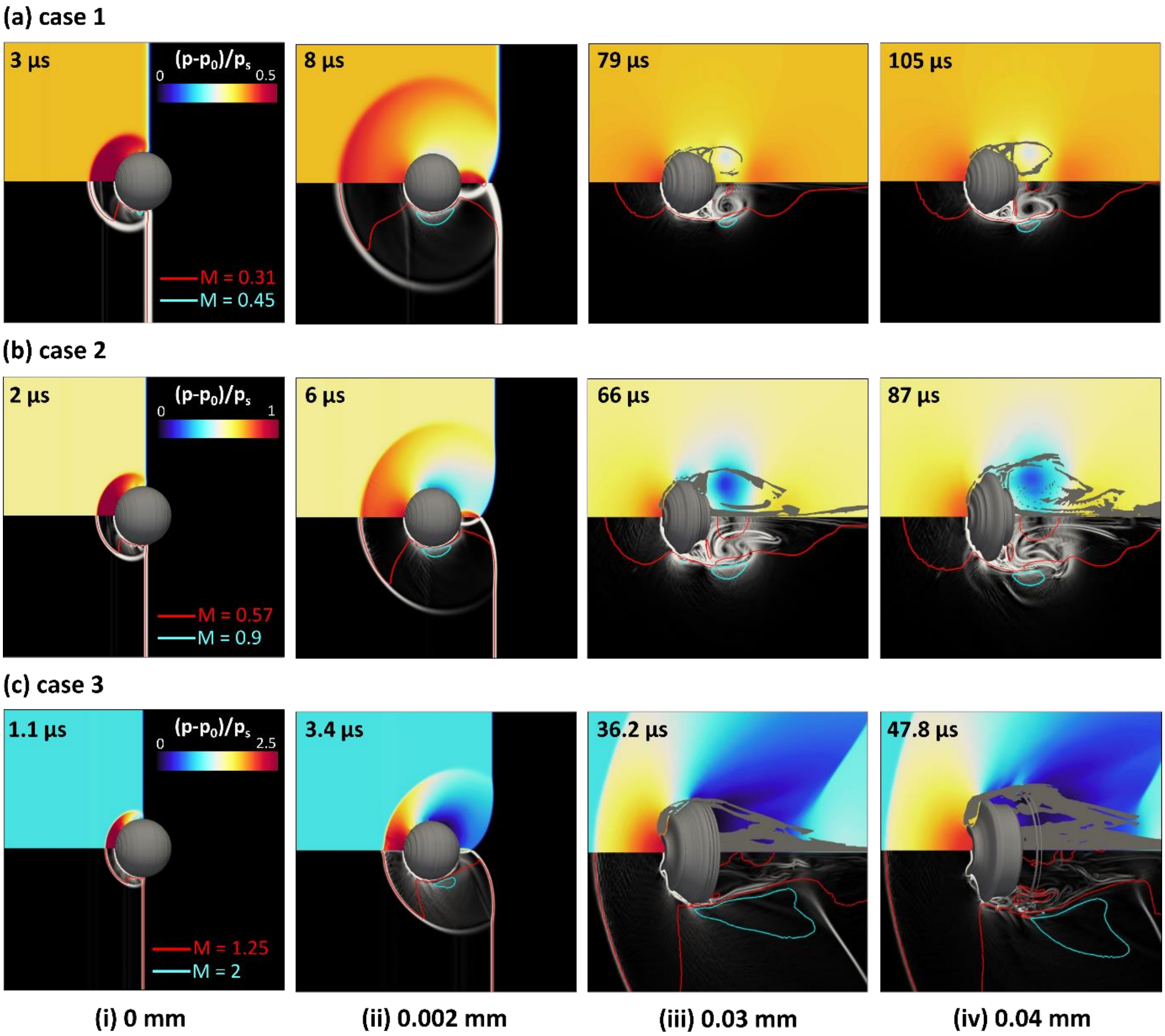

Figure 7 Gas stream conditions during the droplet aerobreakup, while the incident shock wave lies at the same distance from the center of the droplet. Pressure field and produced water mist evolution (top). Numerical schlieren images and Mach number isolines (bottom).

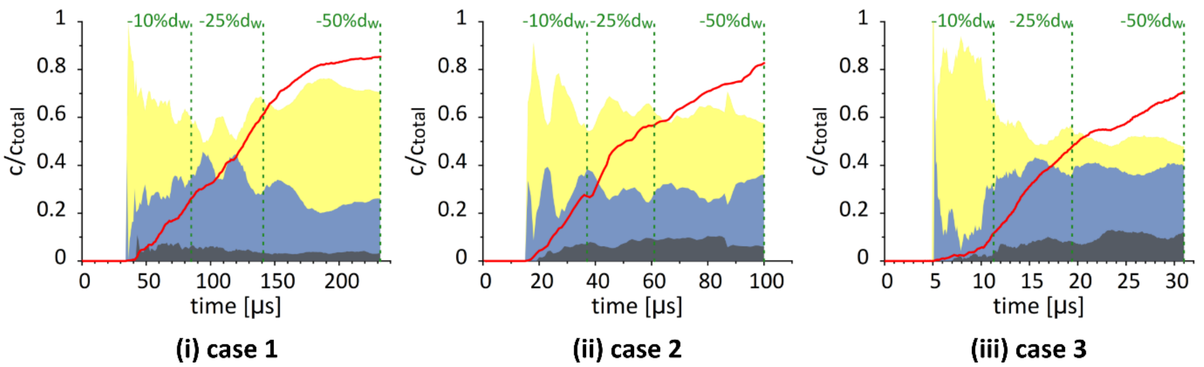

Figure 8 Volume concentration of the secondary droplets with diameters between 5 and 19 µm (gray), 1 and 5 µm (blue), and lower than 1 µm (yellow) over the total volume of the dispersed region. The volume concentration of the dispersed region over the total volume of the water phase is plotted in red. The green vertical lines correspond to a decrease for the width of the deforming droplet by 10%, 25%, and 50%.

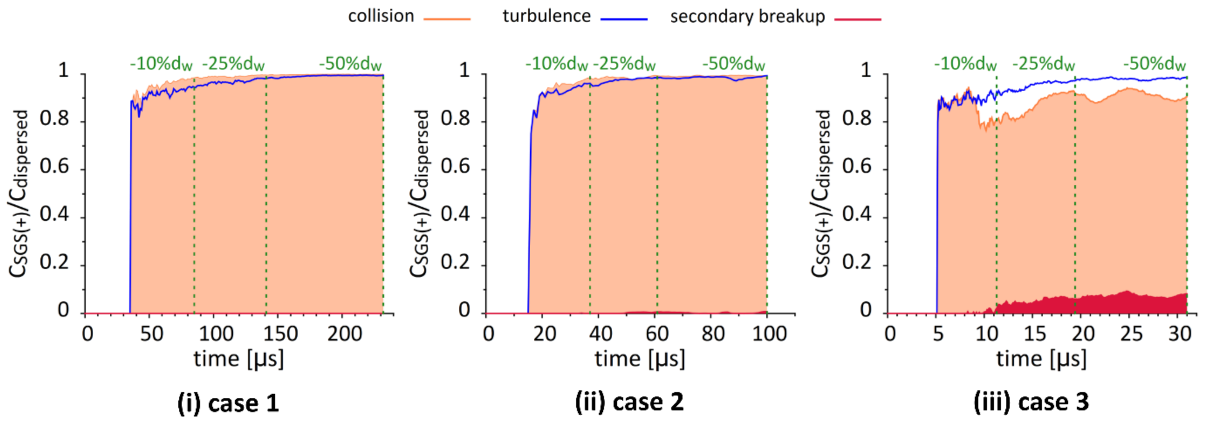

Figure 9 Volume concentration of the subgrid scale mechanisms, namely turbulence, droplet collision, and secondary breakup, that contribute positively to the local interface surface area production and the creation of smaller-scaled droplets over the total volume of the dispersed region. The green vertical lines correspond to a decrease for the width of the deforming droplet by 10%, 25%, and 50%.

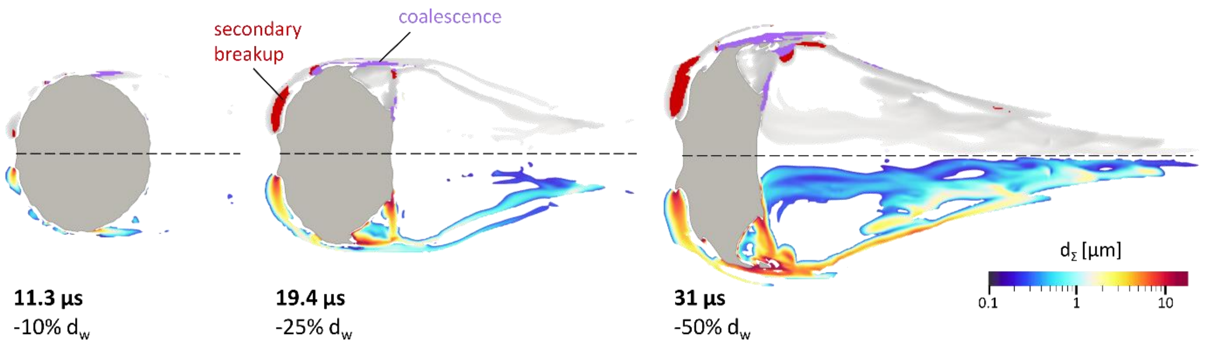

Figure 10 Droplet aerobreakup in case 3 at time instances that correspond to a decrease for the width of the deforming droplet by 10%, 25%, and 50%. Regions in the dispersed mist where the droplet coalescence (purple) and secondary breakup (red) are present (top). Dimensions of the secondary droplets inside the mist (bottom).

IV. CONCLUSION

The aerodynamic breakup of a waterlike droplet under the SIE regime, imposed by three different shock waves with Mach numbers 1.21, 1.46, and 2.64, has been investigated using the proposed multiscale two-fluid approach. The present numerical study provided the opportunity to verify the physical mechanisms of aerobreakup and scrutinize aspects of the process that were not evident in the experimental visualizations of Theofanous [16] and Theofanous et al. [22], using a physically consistent methodology with a viable computational cost. Specifically, the deformation of the coherent droplet interface was fully resolved by the local mesh resolution using the VOF sharp interface method, while the produced mist of secondary fragments was modeled under the diffuse interface approach with consideration of subgrid scale phenomena, namely turbulent mixing, droplet collision and coalescence, and secondary breakup effects.

During the early-stage mist development, two stripping mechanisms were identified to act on the coherent droplet surface. The main stripping mechanism is responsible for the formation of the primary stream of fragments, detached from the droplet equator and the droplet flattened back side, while the secondary stripping mechanism is present on the droplet front side and becomes more significant at supersonic postshock conditions. The largest detached fragments were observed, on average, on the locations of the local liquid stripping and, subsequently, the fragment sizes evolve inside the mist, following the gas stream flow evolution. The postshock flow conditions and the development of a dominant recirculation region behind the deforming droplet play a major role in the formation and expansion of the produced mist. In a supersonic postshock flow, the dispersed mist appears relatively narrower, due to severe aerodynamic conditions that establish a rapid downstream penetration.

Details for the secondary droplets' population and the evolution of the droplets sizes inside the mist were obtained and analyzed based on the modeled subgrid scale phenomena and the local flow development. At supersonic postshock conditions, the coalescence and secondary breakup mechanisms become more pronounced. Additionally, the droplet size distribution is enhanced with larger-scaled droplets even at the later stages of aerobreakup. As a result, the limited mist concentration under supersonic postshock conditions is an outcome of the restricted spanwise expansion of the produced mist and the enhancement of the subgrid scale interface destruction mechanisms inside the mist.

Future research of DNS simulations, which includes the investigation of the produced fragments, can provide a valuable quantitative validation for the present droplet population. Additionally, three-dimensional simulations, using the proposed multiscale two-fluid approach, could be appropriate to reveal more details and mechanisms of the mist dynamics and to consider the significance of three-dimensional phenomena, such as turbulence and vortex shedding, in the droplet aerobreakup.

ACKNOWLEDGMENTS

The research leading to these results has received funding from the European Union's Horizon 2020 Research and Innovation program under the Marie Skłodowska-Curie Grant Agreement No. 675676. The authors gratefully acknowledge the valuable suggestions and help by Dr. Phoevos Koukouvinis during the development of the numerical methodology and the fruitful discussions with Professor Detlef Lohse about the physics of droplet breakup.

APPENDIX: VALIDITY OF CLOSURE MODELS AND NUMERICAL METHOD LIMITATIONS

Modeling limitations may arise in the developed numerical method due to the introduction of closure relations for the source terms in the governing equations, the subgrid scale modeling, the switching criteria within the multiscale framework, and the absence of a quantitative validation for the produced mist. The validity of the utilized models and the imposed assumptions is discussed below, considering specifically the present simulations of droplet aerobreakup and the examined flow conditions.

1) The closure of the interfacial interaction terms, which appear in Navier-Stokes equations after the imposed averaging procedure and consider the mass, momentum, and energy exchange phenomena between the interacting phases, is an inherent modeling requirement of the two-fluid model formulation. In the present simulations, the applied closure relations are consistent with the examined flow conditions, as discussed below.

- In continuity equation (1), the interfacial mass source term, which models the mass transfer due to phase-change phenomena, namely, cavitation and vaporization, is neglected.

    - Cavitation plays a minor role at the early stages of aerobreakup in the examined cases. Specifically, as depicted in Figure 11, in cases 1 and 2 the shock wave propagation evolves smoothly downstream without any significant decrease in the local pressure inside the droplet, which can be related to the development of cavitation regions. On the contrary, in the supersonic case 3, the strong shock wave with Mach number 2.64 results in an increase of the local pressure at 35 bars after impact. At 1.5 μs the propagating shock wave inside the droplet is reflected normal to the droplet outer surface and an expansion wave is created. When the shock wave reaches the back side of the droplet, it partially reflects backwards, and a low-pressure region is formed at 2.5 μs. Similarly, the experimental observations of Sembian et al. [37] depict the creation of cavitation bubbles and the subsequent decrease of the low-pressure region in the aerobreakup of a water column under supersonic conditions. Despite the cavitation development, an early fragmentation, initiating from the back side of the droplet due to cavitation bubbles' collapse, is not observed in the simulation results; the experimental visualizations of Theofanous et al. [22] also confirm the absence of any distinguishable surface oscillations or breakup on the back side of the droplet that can be related to significant cavitation effects.

Since the early stages of the droplet aerobreakup evolution are not driven by cavitation and the minor cavitation region has no macroscopic effect on the droplet fragmentation under the examined conditions, a model for nucleation and subsequent growth of the cavitating bubbles has not been implemented in the numerical framework. Instead, in the supersonic case 3, a very small volume fraction of air of the order of 10^{-6}, which corresponds to a typical nucleation volume fraction [67], is introduced in the initial droplet volume fraction. Under this assumption, the small gaseous volumes inside the droplet will expand after the significant pressure drop, producing expansion similar to those that would occur with cavitation; with the subsequent pressure increase, the gaseous volume gradually collapses, although any condensation and the pressure overshoot effects due to complete vapor collapse (which is not the case with the gas content) are not considered.

- Vaporization modeling is neglected since the local liquid temperature does not increase more than 10 K during the shock wave impact on the droplet in the examined cases. However, vaporization effects can be responsible for the extended water dispersion observed at the later stages of aerobreakup under the supersonic postshock conditions of case 3; thus vaporization could be considered in future research of aerobreakup imposed by high Mach number shock waves.

- Other mass exchange contributions with an effect on interface formation are considered in the transport equation for the interface surface area density Σ, equation (5).

- In momentum equation (2), the interfacial momentum source term accounts for the aerodynamic drag force, which dominates among the other interfacial forces acting between the dispersed droplets and the free-stream gas flow during the aerobreakup process, due to the severe aerodynamic conditions imposed by the upstream and downstream pressure differences. The aerodynamic drag force is defined as $F_D = \frac{1}{2} C_D \rho_{gas} u_r |u_r| A_{droplet}$. The calculated drag coefficient C_D [60] is validated for a vast range of Reynolds numbers and here it is defined based on the local flow properties. The reference area of the droplet $A_{droplet}$ is calculated based on the local interface surface area density Σ. The velocity fields are accurately predicted in the performed simulations, since good agreement between the simulation and experimental results is observed with respect to the overall aerobreakup evolution and the liquid penetration; thus, the relative velocity u_r can be precisely extracted from the two-fluid model.

- In energy equation (3), the interfacial energy source term is modeled via a standard heat transfer law [68] for the calculated temperature fields of the liquid and gaseous phases. In the present simulations, the observed temperature differences between the liquid and gaseous phases on interfacial regions can locally reach the absolute value of 35 K in subsonic case 1, almost 90 K in transonic case 2, and can even exceed the absolute value of 500 K in the bow shock region in supersonic case 3. Therefore, the modeling of thermal effects becomes crucial for the accurate capturing of aerobreakup under high Mach numbers.

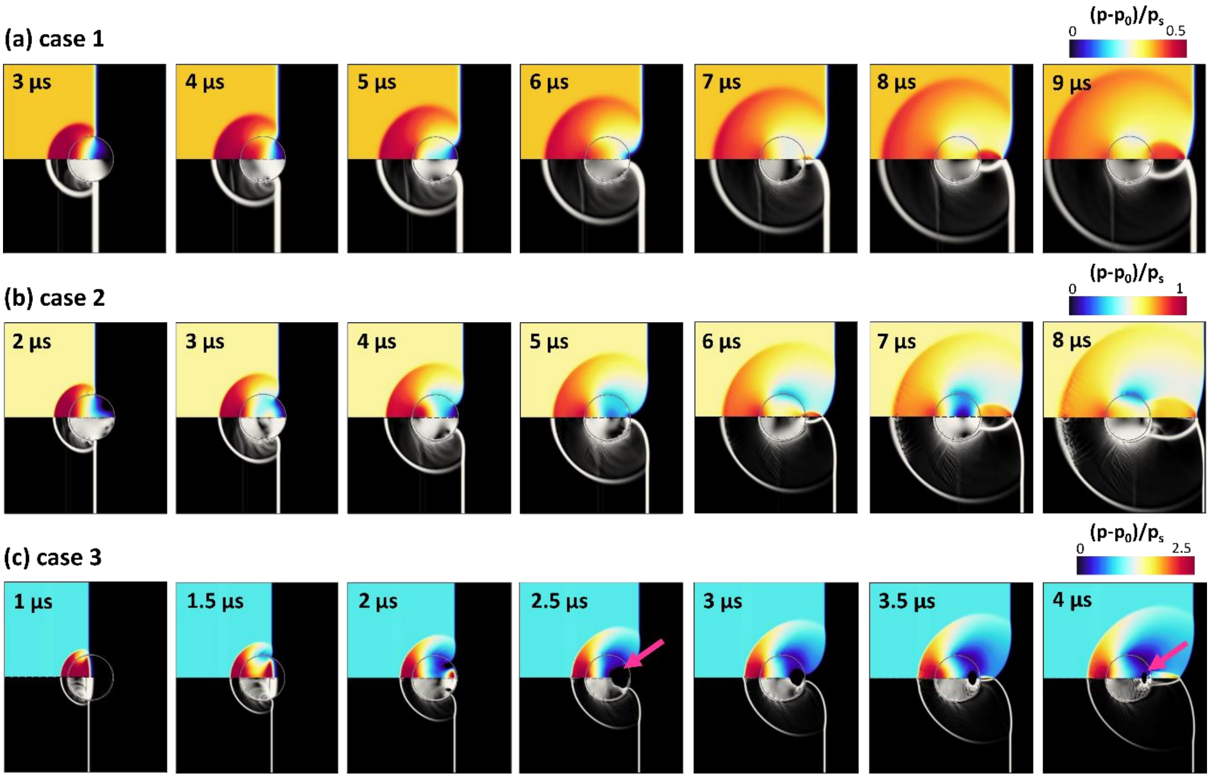

Figure 11 Compressibility effects at the early stages of aerobreakup, namely, the incident shock wave downstream propagation, the reflected shock wave in the free gas stream, and the transmitted shock wave into the liquid droplet. Pressure field (top) and numerical schlieren images (bottom).

2) A fundamental principle of the multiscale two-fluid approach is the subgrid scale modeling of unresolved flow structures via the transport equation for the interface surface area density Σ, equation (5). The physical mechanisms, which are responsible for the interface production and destruction, and which fall below the local mesh resolution, are considered in equation (5) as the subgrid scale source term S_{SGS}. Specifically, the contributions of turbulent flow stretching and wrinkling, along with the subgrid scale droplet interactions, involving droplet collision and coalescence, and secondary breakup effects, are taken into account with the appropriate closure relations, summarized in Table III. The SGS models are a function of the characteristic timescale τ_{SGS} and the critical interface surface area density Σ^*_{SGS} at an equilibrium state between interface production and destruction. The modeling assumptions and the validity of the SGS models are discussed below.

- The turbulence term utilizes the Kolmogorov timescale. The accurate closure of the critical Weber number $\mathrm{We}^*_{\mathrm{turb}}$ [58], which expresses the balance between the liquid kinetic energy and the liquid surface energy at equilibrium state, requires a case-dependent calibration using DNS results. However, considering the significant computational cost, a viable compromise is to set the critical Weber number value equal to 1, even though it may result in a minor underestimation of the effect of turbulence on interface formation, as shown in the DNS study of Duret et al. [69] for the primary atomization of a subsonic spray.

- The collision and coalescence model is based on the particle collision theory [58]. The major assumption concerns the characteristic velocity of collision between the colliding droplets, which is described as a function of the turbulent kinetic energy and has been used in subsonic liquid spray atomization simulations [58], [70]. Due to the lack of any sufficient information regarding the subgrid scale particles and since collision is mainly turbulence driven, the proposed model is acceptable in the present simulations.

- The secondary breakup model is based on the model of Pilch and Erdman [10], developed for Weber numbers up to 10^4. The secondary breakup effects are driven by the mean relative phase velocity [58], which is available within the two-fluid model formulation; thus the relative velocity is directly obtained from the numerical model without the need of further modeling assumptions.

Table III Closure relations for the SGS terms in equation (5) related to interface surface area production and destruction.

SGS mechanism	τ_{SGS}	Σ^*_{SGS}
turbulence	$\frac{k}{\varepsilon}$	$\frac{\alpha_l(1-\alpha_l)\rho_m k_m}{\sigma We^*_{turb}}$ with $We^*_{turb} = 1$ at equilibrium
collision and coalescence	$\frac{1}{\Sigma\sqrt{\frac{2}{3}k_m}}$	$\frac{6\alpha_l(1-\alpha_l)}{d^*_\Sigma}$ with $d^*_\Sigma = d_\Sigma \frac{1+\frac{We^N_{coll}}{6}}{1+\frac{We_{coll}}{6}}$ • critical We for coalescence: $We^N_{coll} = 12$ • relevant We for collision: $We_{coll} = \frac{4\alpha_l(1-\alpha_l)\rho_l k_m}{\sigma\Sigma}$
secondary breakup	$f(We_{BU})\frac{d_\Sigma}{u_r}\sqrt{\frac{\rho_l}{\rho_g}}$ with $We_{BU} = \frac{6\rho_g u_r^2\alpha_l(1-\alpha_l)}{\sigma\Sigma}$	$\frac{6\rho_g u_r^2\alpha_l(1-\alpha_l)}{\sigma We^*_{BU}}$ with $We^*_{BU} = 12(1+1.077Oh^{1.6}) \cong 12$ for Oh << 1

3) The dynamic switching from a sharp to a diffuse interface approach and vice versa, following the implemented criteria in the flow topology detection algorithm, is bounded by the local mesh resolution. In other words, the characteristic dimension, that establishes the resolution capabilities of the multiscale framework and determines which flow structures will be fully resolved and which will be modeled as subgrid scale phenomena, is an external user-defined parameter. Specifically, in the present aerobreakup simulations, the mesh resolution of 100 cells per initial diameter causes droplets with diameters greater than 19 μm to be resolved with the sharp interface approach, while the finer mesh of 200 cells per initial diameter allows for more droplets with a minimum diameter of 9.5 μm to be captured by the local mesh resolution. However, even though the upper limit for the secondary droplets' diameters modeled within the diffuse mist is different for the coarse and the fine mesh, the droplets with diameters in the range of 9.5–19 μm, which are captured by the fine mesh resolution, are not excluded in the coarse mesh predictions. As shown in Figure 12, in the region where the fine mesh detects mesh-resolvable fragments, detached either from the droplet back side or the droplet equator, the coarse mesh identifies the largest-scaled secondary droplets within the diffuse mist.

This switching mechanism operates well with moderate mesh resolutions in multiscale flows like the droplet aerobreakup problem, in which the sizes of the initial coherent droplet and the firstly formed fragments have a difference of approximately two orders of magnitude. However, in flow fields with structures, covering the complete range between microscales to millimeter sizes, the switching mechanisms should be improved. Part of the ongoing research is the coupling of an adaptive mesh refinement algorithm with the sharp interface formulation in order to accurately capture the intermediate-scaled structures that are part of the sharp interface formulation, and the original moderate mesh is insufficient to resolve.

Overall, the mesh dependency of the switching criteria does not imply a mesh-dependent numerical solution in the aerobreakup simulations. A <u>mesh independence investigation</u> is shown in Figure 13, comparing the development of the dispersed region over time for the three examined cases of Table II, using a computational mesh of 100 and 200 cells per initial diameter. For consistency between the two mesh resolutions, the coarser simulation of 100 cells per diameter includes droplets up to 9.5 μm, which corresponds to the local mesh resolution and, thus, the upper limit for the dispersed region resolution with the finer mesh. In cases 1 and 2 very good agreement between the different mesh resolutions is observed, while in case 3 a small deviation of about 10% is noticeable at the early stages of aerobreakup. Considering that any small deviation is enhanced by microscale droplets below 1 μm, it is safe to conclude that the proposed numerical method is independent of the computational mesh.

4) A <u>quantitative validation</u> for the mist dynamics and the sizes of the underlying secondary droplets is restricted by the visualization capabilities inside the dense mist. In the experiments of Theofanous [16] and Theofanous et al. [22], the utilized camera resolution of 5μm/pixel does not allow for the quantification of smaller droplet sizes, which are illustrated as a dilute cloud of undefined and shapeless structures. Thus, the extraction of any information regarding the droplet sizes inside the dense mist is not feasible in the available experimental visualizations. To the best of the authors' knowledge, size distributions for the produced fragments after the droplet aerobreakup are available in the literature to date, but only in experimental studies of moderate droplet fragmentation cases [27], [28], [29], [30], [31] in the transition zone between the RTP and SIE regimes. In these cases, the fragments form as a part of a distinguishable liquid trace behind the deforming droplet and not as individual small structures inside a dense and hazy cloud; thus the visualization of the underlying structures is significantly more pronounced, and a quantitative analysis of the produced fragments is achievable with the use of advanced visualization techniques.

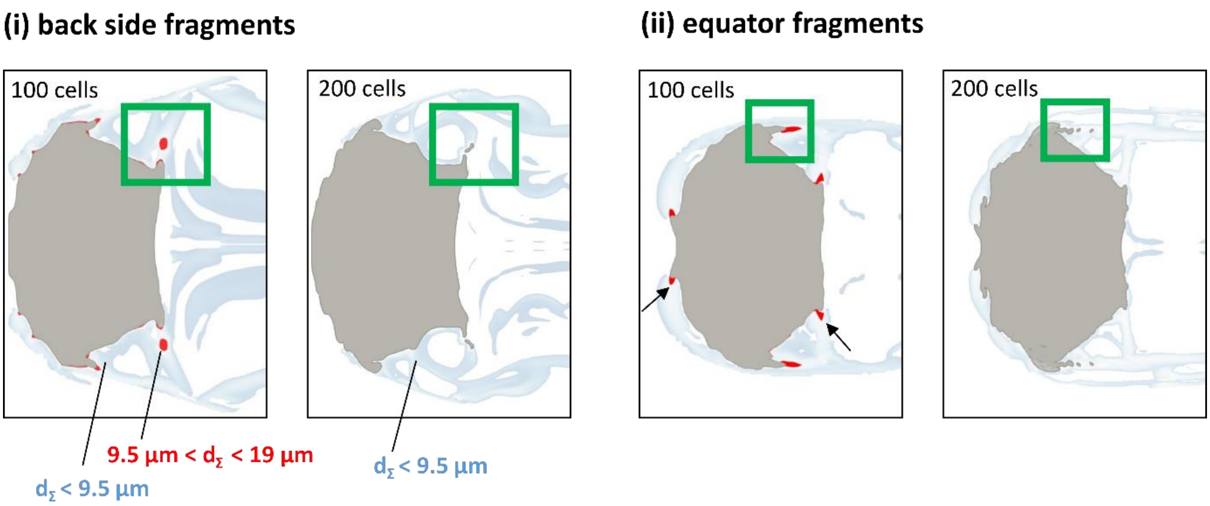

Figure 12 Demonstration of the upper limit for the secondary droplets' diameters modeled within the diffuse mist, using a computational mesh with a resolution of 100 and 200 cells per original diameter. Illustrated in blue are the secondary droplets inside the mist, captured with both mesh resolutions. Illustrated in red are the droplets that are modeled inside the mist with the coarse mesh but are resolved by the mesh resolution with the fine mesh, shown inside the green box. The arrows point to areas where the coarse mesh detects fragments due to the unresolved interface sharpness.

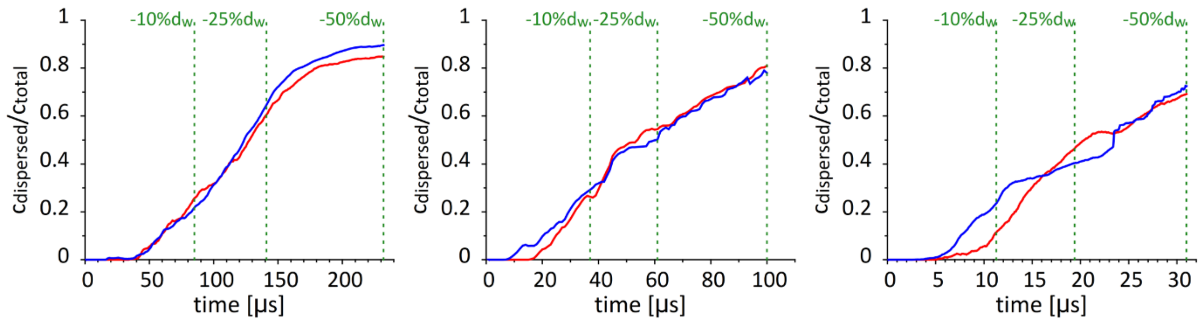

(i) case 1 **(ii) case 2** **(iii) case 3**

Figure 13 Volume concentration of the dispersed region over the total volume of the water phase for a mesh resolution of 100 (red solid line) and 200 (blue solid line) cells per initial droplet diameter. The green vertical lines correspond to a decrease for the width of the deforming droplet by 10%, 25%, and 50%.

REFERENCES

[1] D. R. Guildenbecher, C. Lopez-Rivera, and P. E. Sojka, *Secondary Atomization*, Exp. Fluids **46**, 371 (2009).

[2] R. D. Reitz and R. Diwakar, *Effect of Drop Breakup on Fuel Sprays*, SAE Trans. **95**, 218 (1986).

[3] E. Abo-Serie, C. Arcoumanis, and M. Gavaises., *Spray Characterisation of Swirl Pressure Atomizers for G-DI Engines: Phase Doppler Measurements.*, in *Proceedings of ILASS-Europe, Darmstadt, Germany* (2000), pp. 11–13.

[4] A. E. S. E. T. Alajmi, N. M. Adam, A. A. Hairuddin, and L. C. Abdullah, *Fuel Atomization in Gas Turbines: A Review of Novel Technology*, Int. J. Energy Res. **43**, 3166 (2019).

[5] M. A. Benjamin, R. J. Jensen, and M. Arienti, *Review of Atomization: Current Knowledge and Future Requirements for Propulsion Combustors*, At. Sprays **20**, 485 (2010).

[6] R. N. Dahms and J. C. Oefelein, *Atomization and Dense-Fluid Breakup Regimes in Liquid Rocket Engines*, J. Propuls. Power **31**, 1221 (2015).

[7] B. E. Gelfand, *Droplet Breakup Phenomena in Flows with Velocity Lag*, Prog. Energy Combust. Sci. **22**, 201 (1996).

[8] O. Gohardani, *Impact of Erosion Testing Aspects on Current and Future Flight Conditions*, Prog. Aerosp. Sci. **47**, 280 (2011).

[9] J. O. Hinze, *Fundamentals of the Hydrodynamic Mechanism of Splitting in Dispersion Processes*, AIChE J. **1**, 289 (1955).

[10] M. Pilch and C. A. Erdman, *Use of Breakup Time Data and Velocity History Data to Predict the Maximum Size of Stable Fragments for Acceleration-Induced Breakup of a Liquid Drop*, Int. J. Multiph. Flow **13**, 741 (1987).

[11] G. M. Faeth, L.-P. Hsiang, and P.-K. Wu, *Structure and Break-up Properties of Sprays*, Int. J. Multiph. Flow **21**, 99 (1995).

[12] D. Stefanitsis, G. Strotos, N. Nikolopoulos, E. Kakaras, and M. Gavaises, *Improved Droplet Breakup Models for Spray Applications*, Int. J. Heat Fluid Flow **76**, 274 (2019).

[13] D. Stefanitsis, G. Strotos, N. Nikolopoulos, and M. Gavaises, *Numerical Investigation of the Aerodynamic Breakup of a Parallel Moving Droplet Cluster*, Int. J. Multiph. Flow **121**, 103123 (2019).

[14] D. Stefanitsis, I. Malgarinos, G. Strotos, N. Nikolopoulos, E. Kakaras, and M. Gavaises, *Numerical Investigation of the Aerodynamic Breakup of Droplets in Tandem*, Int. J. Multiph. Flow **113**, 289 (2019).

[15] T. G. Theofanous, G. J. Li, and T. N. Dinh, *Aerobreakup in Rarefied Supersonic Gas Flows*, J. Fluids Eng. **126**, 516 (2004).

[16] T. G. Theofanous, *Aerobreakup of Newtonian and Viscoelastic Liquids*, Annu. Rev. Fluid Mech. **43**, 661 (2011).

[17] O. G. Engel, *Fragmentation of Waterdrops in the Zone behind an Air Shock*, J. Res. Natl. Bur. Stand. U.S. **60**, 245 (1958).

[18] J. A. Nicnolls and A. A. Ranger, *Aerodynamic Shattering of Liquid Drops*, AIAA J. **7**, 285 (1969).

[19] A. Wierzba and K. Takayama, *Experimental Investigation of the Aerodynamic Breakup of Liquid Drops*, AIAA J. **26**, 1329 (1988).

[20] T. Yoshida and K. Takayama, *Interaction of Liquid Droplets with Planar Shock Waves*, J. Fluids Eng. Trans. ASME **112**, 481 (1990).

[21] T. G. Theofanous and J. G. Li, *On the Physics of Aerobreakup*, Phys. Fluids **20**, 052103 (2008).

[22] T. G. Theofanous, V. V. Mitkin, C. L. Ng, C. H. Chang, X. Deng, and S. Sushchikh, *The Physics of Aerobreakup. II. Viscous Liquids*, Phys. Fluids **24**, 022104 (2012).

[23] T. G. Theofanous, V. V. Mitkin, and C. L. Ng, *The Physics of Aerobreakup. III. Viscoelastic Liquids*, Phys. Fluids **25**, 032101 (2013).

[24] V. V. Mitkin and T. G. Theofanous, *The Physics of Aerobreakup. IV. Strain-Thickening Liquids*, Phys. Fluids **29**, 122101 (2017).

[25] Z. Wang, T. Hopfes, M. Giglmaier, and N. A. Adams, *Effect of Mach Number on Droplet Aerobreakup in Shear Stripping Regime*, Exp. Fluids **61**, 1 (2020).

[26] D. Hébert, J.-L. Rullier, J.-M. Chevalier, I. Bertron, E. Lescoute, F. Virot, and H. El-Rabii, *Investigation of Mechanisms Leading to Water Drop Breakup at Mach 4.4 and Weber Numbers above 105*, SN Appl. Sci. **2**, 1 (2020).

[27] L. P. Hsiang and G. M. Faeth, *Near-Limit Drop Deformation and Secondary Breakup*, Int. J. Multiph. Flow **18**, 635 (1992).

[28] L. P. Hsiang and G. M. Faeth, *Drop Properties after Secondary Breakup*, Int. J. Multiph. Flow **19**, 721 (1993).

[29] L. P. Hsiang and G. M. Faeth, *Droplet Deformation Due To Shock Wave and Steady Disturbances*, Int. J. Multiph. Flow **21**, 545 (1995).

[30] E. Villermaux, *Fragmentation*, Ann. Rev. Fluid Mech. **39**, 419 (2007).

[31] Z. Xu, T. Wang, and Z. Che, *Droplet Deformation and Breakup in Shear Flow of Air*, Phys. Fluids **32**, 052109 (2020).

[32] H. Chen, *Two-Dimensional Simulation of Stripping Breakup of a Water Droplet*, AIAA J. **46**, 1135 (2008).

[33] R. Saurel and R. Abgrall, *Simple Method for Compressible Multifluid Flows*, SIAM J. Sci. Comput. **21**, 1115 (1999).

[34] D. Igra and K. Takayama, *A Study of Shock Wave Loading on a Cylindrical Water Column*, Rep.

Inst. Fluid Sci. Tohoku Univ. **13**, 19 (2001).

[35] G. Allaire, S. Clerc, and S. Kokh, *A Five-Equation Model for the Simulation of Interfaces between Compressible Fluids*, J. Comput. Phys. **181**, 577 (2002).

[36] J. C. Meng and T. Colonius, *Numerical Simulations of the Early Stages of High-Speed Droplet Breakup*, Shock Waves **25**, 399 (2015).

[37] S. Sembian, M. Liverts, N. Tillmark, and N. Apazidis, *Plane Shock Wave Interaction with a Cylindrical Water Column*, Phys. Fluids **28**, 056102 (2016).

[38] H. Yang and J. Peng, *Numerical Study of the Shear-Thinning Effect on the Interaction between a Normal Shock Wave and a Cylindrical Liquid Column*, Phys. Fluids **31**, 043101 (2019).

[39] J. W. J. Kaiser, J. M. Winter, S. Adami, and N. A. Adams, *Investigation of Interface Deformation Dynamics during High-Weber Number Cylindrical Droplet Breakup*, Int. J. Multiph. Flow **132**, 103409 (2020).

[40] D. Igra and K. Takayama, *Numerical Simulation of Shock Wave Interaction with a Water Column*, Shock Waves **11**, 219 (2001).

[41] D. Igra and K. Takayama, *Investigation of Aerodynamic Breakup of a Cylindrical Water Droplet*, At. Sprays **11**, 167 (2001).

[42] J. C. Meng and T. Colonius, *Numerical Simulation of the Aerobreakup of a Water Droplet*, J. Fluid Mech. **835**, 1108 (2018).

[43] N. Liu, Z. Wang, M. Sun, H. Wang, and B. Wang, *Numerical Simulation of Liquid Droplet Breakup in Supersonic Flows*, Acta Astronaut. **145**, 116 (2018).

[44] D. Stefanitsis, P. Koukouvinis, N. Nikolopoulos, and M. Gavaises, *Numerical Investigation of the Aerodynamic Droplet Breakup at Mach Numbers Greater Than 1*, J. Energy Eng. **147**, 04020077 (2021).

[45] J. W. J. Kaiser, D. Appel, F. Fritz, S. Adami, and N. A. Adams, *A Multiresolution Local-Timestepping Scheme for Particle–Laden Multiphase Flow Simulations Using a Level-Set and Point-Particle Approach*, Comput. Methods Appl. Mech. Eng. **384**, 113966 (2021).

[46] C. H. Chang, X. Deng, and T. G. Theofanous, *Direct Numerical Simulation of Interfacial Instabilities: A Consistent, Conservative, All-Speed, Sharp-Interface Method*, J. Comput. Phys. **242**, 946 (2013).

[47] B. Dorschner, L. Biasiori-Poulanges, K. Schmidmayer, H. El-Rabii, and T. Colonius, *On the Formation and Recurrent Shedding of Ligaments in Droplet Aerobreakup*, J. Fluid Mech. **904**, A20 (2020).

[48] M. Jalaal and K. Mehravaran, *Fragmentation of Falling Liquid Droplets in Bag Breakup Mode*, Int. J. Multiph. Flow **47**, 115 (2012).

[49] M. Jain, R. S. Prakash, G. Tomar, and R. V. Ravikrishna, *Secondary Breakup of a Drop at Moderate Weber Numbers*, Proc. R. Soc. A Math. Phys. Eng. Sci. **471**, 20140930 (2015).

[50] G. Nykteri, P. Koukouvinis, R. S. Gonzalez Avila, C.-D. Ohl, and M. Gavaises, *A Σ-Y Two-Fluid Model with Dynamic Local Topology Detection : Application to High-Speed Droplet Impact*, J. Comput. Phys. **408**, 109225 (2020).

[51] A. Andreini, C. Bianchini, S. Puggelli, and F. X. Demoulin, *Development of a Turbulent Liquid Flux Model for Eulerian-Eulerian Multiphase Flow Simulations*, Int. J. Multiph. Flow **81**, 88 (2016).

[52] N. Bremond and E. Villermaux, *Bursting Thin Liquid Films*, J. Fluid Mech. **524**, 121 (2005).

[53] X. K. Cao, Z. G. Sun, W. F. Li, H. F. Liu, and Z. H. Yu, *A New Breakup Regime of Liquid Drops Identified in a Continuous and Uniform Air Jet Flow*, Phys. Fluids **19**, 057103 (2007).

[54] M. Ishii and K. Mishima, *Two-Fluid Model and Hydrodynamic Constitutive Relations*, Nucl. Eng. Des. **82**, 107 (1984).

[55] A. Vallet and R. Borghi, *Modelisation Eulerienne de l'atomisation d'un Jet Liquide*, Comptes Rendus l'Académie Des Sci. IIB-Mechanics-Physics-Astronomy **327**, 1015 (1999).

[56] C. W. Hirt and B. D. Nichols, *Volume of Fluid (VOF) Method for the Dynamics of Free Boundaries*, J. Comput. Phys. **39**, 201 (1981).

[57] R. Scardovelli and S. Zaleski, *Direct Numerical Simulation of Free-Surface and Interfacial Flow*, Annu. Rev. Fluid Mech. **31**, 567 (1999).

[58] R. Lebas, T. Menard, P. A. Beau, A. Berlemont, and F. X. Demoulin, *Numerical Simulation of Primary Break-up and Atomization: DNS and Modelling Study*, Int. J. Multiph. Flow **35**, 247 (2009).

[59] J. U. Brackbill, D. B. Kothe, and C. Zemach, *A Continuum Method for Modeling Surface Tension*, J. Comput. Phys. **100**, 335 (1992).

[60] G. I. Kelbaliyev, *Drag Coefficients of Variously Shaped Solid Particles, Drops, and Bubbles*, Theor. Found. Chem. Eng. **45**, 248 (2011).

[61] S. S. Deshpande, L. Anumolu, and M. F. Trujillo, *Evaluating the Performance of the Two-Phase Flow Solver InterFoam*, Comput. Sci. Discov. **5**, 014016 (2012).

[62] A. Vallet, A. A. Burluka, and R. Borghi, *Development of a Eulerian Model for the "Atomization" of a Liquid Jet*, At. Sprays **11**, (2001).

[63] J. Chesnel, J. Reveillon, T. Menard, and F. X. Demoulin, *Large Eddy Simulation of Liquid Jet Atomization*, At. Sprays **21**, 711 (2011).

[64] R. T. Lahey, *The Simulation of Multidimensional Multiphase Flows*, Nucl. Eng. Des. **235**, 1043 (2005).

[65] D. Stefanitsis, I. Malgarinos, G. Strotos, N. Nikolopoulos, E. Kakaras, and M. Gavaises, *Numerical Investigation of the Aerodynamic Breakup of Diesel and Heavy Fuel Oil Droplets*, Int. J. Heat Fluid Flow **68**, 203 (2017).

[66] M. J. Ivings, D. M. Causon, and E. F. Toro, *On Riemann Solvers for Compressible Liquids*, Int. J. Numer. Methods Fluids **28**, 395 (1998).

[67] S. Karthika, T. K. Radhakrishnan, and P. Kalaichelvi, *A Review of Classical and Nonclassical Nucleation Theories*, Cryst. Growth Des. **16**, 6663 (2016).

[68] W. E. Ranz and W. R. Marshall, *Evaporation from Drops - Part I*, Chem. Eng. Prog. **48**, 141 (1952).

[69] B. Duret, J. Reveillon, T. Menard, and F. X. Demoulin, *Improving Primary Atomization Modeling through DNS of Two-Phase Flows*, Int. J. Multiph. Flow **55**, 130 (2013).

[70] T. F. Leung, C. P. Groth, and J. Hu, *Evaluation of an Eulerian-Lagrangian Spray Atomization (ELSA) Model for Nozzle Flow: Modeling of Coupling Between Dense and Disperse Regions*, in *47th AIAA Thermophysics Conference* (2017), p. 4352.